

# 博士論文（要約）

Studies on preparation and characterization of zinc  
oxide/TEMPO-oxidized cellulose nanofiber composite films

(酸化亜鉛／**TEMPO** 酸化セルロースナノファイバー  
複合化フィルムの調製と特性解析に関する研究)

ニン    ルイジ

Ning    Ruizhi

寧    芮之

# Table of Contents

Chapter 1 General Introduction .....	4
1.1 Nanocellulose .....	4
1.1.1 Cellulose .....	4
1.1.2 Nanocellulose .....	6
1.1.3 TEMPO-oxidized cellulose nanofibers .....	9
1.2 CNF-based composites .....	11
1.2.1 CNF reinforced polymer composites .....	11
1.2.2 Functional composites of inorganic/CNF .....	12
1.3 Zinc oxide/nanocellulose composites .....	12
1.3.1 Zinc oxide .....	12
1.3.2 Preparation of zinc oxide/nanocellulose nanocomposites .....	13
1.3.3 Multiple functions of zinc oxide/nanocellulose composites .....	14
1.4 Research objectives .....	18
1.5 References .....	19
Chapter 2 Preparation of ZnO/TOCN nanocomposite films and property investigation of the films with different ZnO contents .....	27
2.1 Abstract .....	27
2.2 Introduction .....	27
2.3 Materials and methods .....	29
2.3.1 Materials .....	29
2.3.2 Preparation of TOCN dispersion .....	29
2.3.3 ZnO/TOCN composite films .....	29
2.3.4 Characterization .....	30
2.4 Results and discussion .....	31
2.4.1 Fundamental properties .....	31
2.4.2 Optical properties of ZnO/TOCN composite films .....	35
2.4.3 Thermal properties of ZnO/TOCN composite films .....	36
2.4.4 Surface hydrophilic and hydrophobic properties of ZnO/TOCN composite films .....	38
2.4.5 Mechanical properties .....	40

2.4.6 Antimicrobial activity.....	41
2.5 Conclusions .....	42
2.6 Appendix .....	43
2.7 References .....	47
Chapter 3 Influences of the morphology of ZnO nanoparticles on films properties of ZnO/TOCN composites.....	50
3.1 Abstract .....	50
3.2 Introduction .....	50
3.3 Materials and methods.....	51
3.3.1 Materials.....	51
3.3.2 Preparation of ZnO/TOCN nanocomposite films.....	52
3.3.3 Characterization of ZnO particles and ZnO/TOCN composite films.....	52
3.3.4 UV-induced catalytic degradation of MB in water.....	53
3.4 Results and discussion.....	53
3.4.1 Fundamental properties .....	53
3.4.2 Thermal and mechanical properties.....	57
3.4.3 Hydrophilicity and oxygen permeability .....	59
3.4.4 Optical properties .....	60
3.4.5 UV and ZnO-induced catalytic degradation of MB .....	61
3.5 Conclusions .....	63
3.6 Appendix .....	65
3.7 References .....	69
Chapter 6 Summary.....	71
Publications .....	74

# Chapter 1

## General Introduction

### 1.1 Nanocellulose

#### 1.1.1 Cellulose

Cellulose is the most common polysaccharide biosynthesized in nature, the total annual biomass production of which is estimated about 1.5 trillion tons [1]. Therefore, cellulose is the most competitive material for making sustainable and biocompatible products. Cellulose can be biosynthesized by certain species of bacteria, tunicates and plants. Among those, plant cell walls are the main resource of cellulose. Cellulose has a hierarchical structure in woods [1–3]. As shown in Figure 1.1, cellulose fibers are composed of bundles of cellulose fibrils, which are formed by crystalline cellulose microfibrils 3–4 nm wide consisting of 30–40 cellulose chains [3].

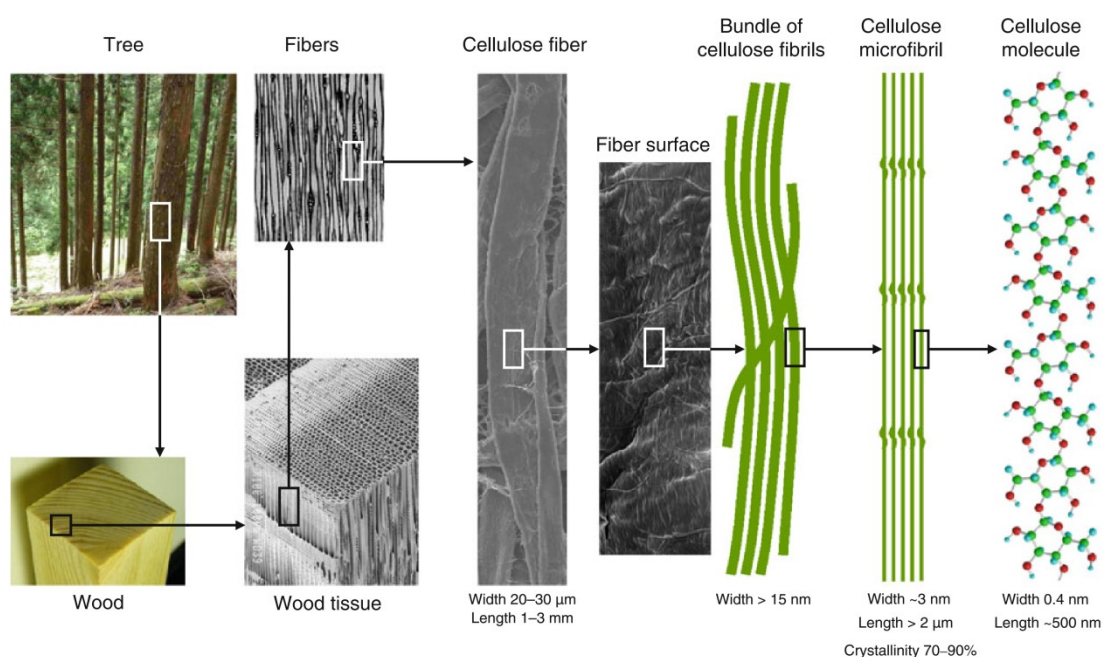


**Figure 1.1.** The hierarchical structure of wood cellulose. [2]

The cellulose chain is a linear homopolymer consisting of  $\beta$ -1,4-linked D-glucopyranose units. As shown in Figure 1.2, successive glucose residues are inverted 180°, leading to a flat ribbon structure in



which the repeating unit is cellobiose [4]. Extensive hydrogen bonds and van der Waal forces existing between parallel individual cellulose chains result in crystallization of cellulose chains into microfibrils. In plants, the enzyme complex (cellulose synthase, CelS) presented on plant plasma membranes is responsible for the synthesis of cellulose. By far, the cloning of the CesA genes has been presumed to encode catalytic subunits of CelS [4–6]. Electron microscopy in freeze-fractured plasma membranes of many organisms has identified hexagonal structures with six-fold symmetry, termed rosettes, in mosses, ferns, algae and vascular plants. As shown in Figure 1.3, in a 6×6 chain model, six rosette subunits, possibly containing six CesA polypeptides, interact to form a rosette, a single CesA enzyme complex. Each CesA polypeptide is shown to be involved in the synthesis of one  $\beta$ -1,4-glucan chain [4]. Cellulose chains crystallize as it synthesizes [4,6], because of the extensive hydrogen bonds and van der Waal forces existing between parallel individual cellulose chains. It results in crystallization of cellulose chains into microfibrils. Therefore, native cellulose is always in the form of microfibrils.

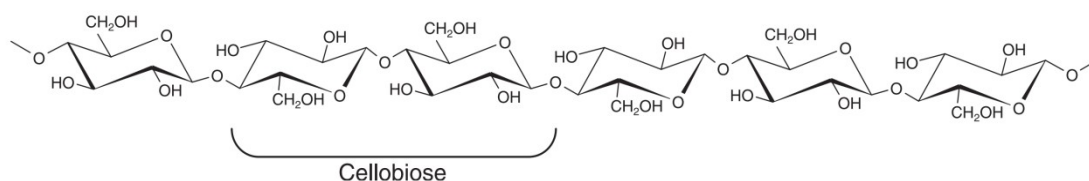


**Figure 1.2.** Inversion of adjacent glucose residues in a  $\beta$ -1,4- glucan fragment. [6]

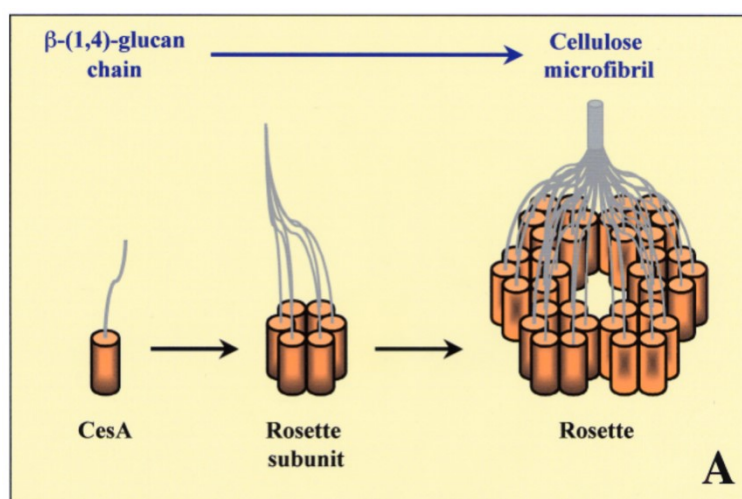


**Figure 1.3.** A 6×6 chain model for the structure of the rosette in biosynthesis of cellulose. [4]

Cellulose can exist as the crystalline microfibrils of cellulose I, II, III, and IV [7]. The crystal transition for cellulose brings the skeletal contraction accompanied with the change in intramolecular

hydrogen bonds, thus lead to a drastic change in the crystal modulus. Table 1.1 exhibits the elastic modulus  $E_l$  of the crystalline regions in the direction parallel to the chain axis measured by x-ray diffraction reported by Nishino [8]. The result illustrated that the native cellulose I is decidedly stiffer and stronger than the “man-made” forms. Native cellulose microfibrils with the form of cellulose I [7,9,10] have high crystal moduli of 110-150 GPa [11–13] and high strength of 2-3 GPa [12].

**Table 1.1.**  $E_l$ -value of cellulose polymorphs. [8]

	$E_l$ (GPa)
I	138
II	88
III <sub>I</sub>	87
III <sub>II</sub>	58
IV <sub>I</sub>	75

### 1.1.2 Nanocellulose

Nanocellulosic materials can be divided into three main categories: bacteria cellulose (BC), cellulose nanocrystals (CNC) and cellulose nanofibrils (CNF). CNF has been previous described as microfibrillated cellulose (MFC) or nanofibrillated cellulose (NFC).

#### *Bacteria cellulose*

BC fibers are secreted extracellularly by certain bacteria (notably *Acetobacter xylinum*) [14,15]. BC is the only pure form of cellulose in nature, because no other components are synthesized with cellulose [15–17]. The secreted BC is ribbon-shaped fibrils with width of less than 100 nm, which is composed of much finer 2-4 nm nanofibrils [15,18,19] (Figure 1.4). Compared with plant cellulose, BC have high crystallinity up to 84-89% and higher degree of polymerization up to 8000, finer web-like network and consequent higher water holding capacity ~97% [16,17,20–22].

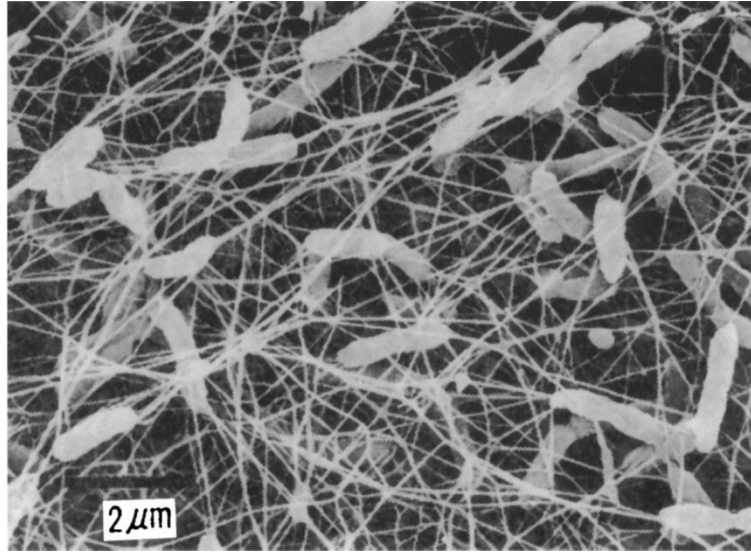


**Figure 1.4.** Scanning electron microscope (SEM) image of BCs. [15]

#### *Cellulose nanocrystal*

Crystallographic data presents evidence that cellulose within microfibrils is not perfectly crystalline [23–25]. Nishiyama et al. represented direct evidence for small disordered regions that are periodically distributed along the cellulose microfibrils of higher plants by small angle neutron scattering [26]. They reported that the microfibrils can be considered to have 4-5 disordered residues every 300 residues. Therefore, through controlled acid hydrolysis, the disordered segments can be selectively hydrolysed and finally reach to the level-off degree of polymerization [27–30]. The remained rod-like or whisker-shaped particles are named CNC, which is shown in Figure 1.5. CNCs have high aspect ratio (3-5 nm in width, 50-500 nm in length) and high crystallinity (54-88%) [31]. Sulphuric acid hydrolysis is the predominant method for CNC preparation. When prepared with sulfuric acid, organic sulphate groups are introduced on the CNC surface, which give rise to electrostatic repulsion and stable suspension in water [32]. However, CNC yield with the normal sulphuric acid hydrolysis is often <30% [33,34] and both width and length have wide distribution [35,36]. Besides sulphuric acid, hydrochloric acid (HCl) [37] and phosphoric acid [38] have been used as the hydrolyzing acid. The HCl hydrolysis leaves the crystallite uncharged and makes the prepared CNCs have no colloidal stability in aqueous environment [37].

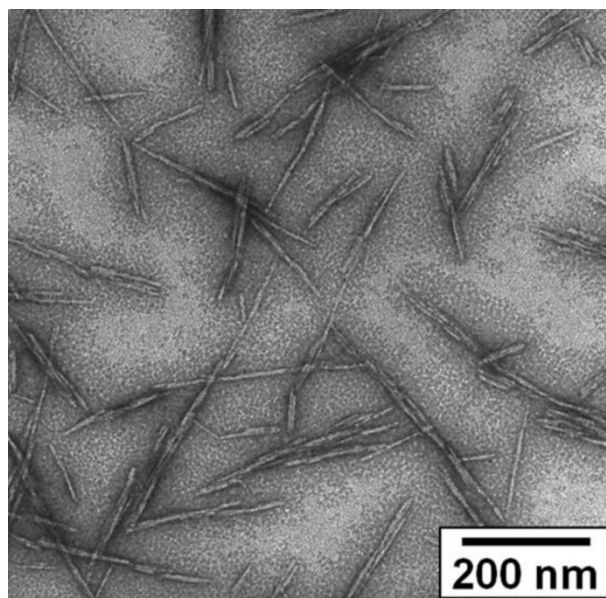


**Figure 1.5.** Transmission electron microscope (TEM) image of CNCs. [31]

#### *Cellulose nanofibrils*

CNFs are nano-sized thin flexible fibrils, encompassing both the crystalline and disordered domains with 5-50 nm width and length within the micron scale [39]. To extract CNF from natural resources, two distinctive methods are available: mechanical disintegration and chemistry-assisted nanofibrillation [3]. Industrial production of MFC has been carried out by repeated high-pressure homogenization using dilute slurries of refined cellulose fibers. The prepared products are MFC aggregates with fibril structures with diameters between 20-100 nm and estimated lengths of several tens of micrometers [40–43] (Figure 1.6a). The hemicelluloses content [44] and raw materials of cellulose [45] have been reported to make a difference on the MFC morphology. However, the intensive mechanical disintegration process require high energy consumption (70,000 kWh/tonne [46]) and complete individualization of wood cellulose fibers to NFC with 3-4 nm width by only mechanical disintegration has not yet been achieved [2]. The combination of mechanical disintegration and certain pretreatments could significantly decrease the energy consumption (1,000 kWh/tonne [47]), such as enzyme-assisted hydrolysis [48–50] and oxidation pre-treatments [51,52] (Figure 1.6b and c). In particular, 2,2,6,6-tetramethylpiperidine-1-oxyl (TEMPO)-mediated oxidation in a water system achieved the introduction of abundant anionic groups on microfibril surfaces and complete individualization of CNFs with uniform 3 nm width after mild mechanical treatment [3].

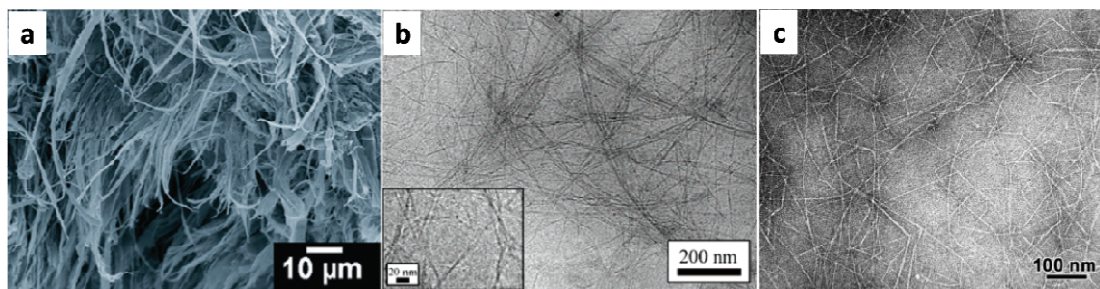


**Figure 1.6.** (a) SEM image of MFC prepared by high-pressure homogenization, [43] and TEM images of NFC prepared with (b) enzyme-assisted hydrolysis [48] and (c) TEMPO-mediated oxidation [52] followed by mechanical treatments.

### 1.1.3 TEMPO-oxidized cellulose nanofibers

In 1995, de Nooy et al. reported the highly selective oxidation of primary alcohol groups in water-soluble polysaccharide by catalytic amount of TEMPO and hypochlorite/bromide as the regenerating oxidant in water [53]. Three years later, Isogai carried out the TEMPO/NaBr/NaClO system on various cellulose samples [54], which laid a foundation for the preparation of new CNFs. Then in 2006, Saito et al. successfully prepared homogenous suspensions of individualized CNFs from TEMPO-oxidized native cellulose [52].

The C6 primary hydroxyls of cellulose are expected to be oxidized to C6 carboxylate groups by TEMPO/NaBr/NaClO oxidation in water at pH 10–11. The hypothesis of the oxidation process [55–57] is shown in Figure 1.7. When native celluloses were subjected to TEMPO-mediated oxidation, the original fibrous morphologies and crystal structures are unchanged even under harsh oxidation conditions or for extended reaction times. However, significant amounts of sodium carboxylate groups and small amounts of aldehyde groups are formed in the products by oxidation of a part of C6 primary hydroxyls [58]. Due to the dissociation of carboxylate groups on cellulose surfaces in water, electric double layer repulsion is generated between the surface oxidized microfibrils. When the surface carboxylate contents of bleached hardwood and softwood kraft pulps were more than approximately 0.8 mmol g<sup>-1</sup>, the oxidized cellulose/water slurries can be mostly converted to transparent and highly viscous dispersions by the mild mechanical disintegration treatment using a household blender, double-cylinder-type homogenizer or ultrasonic homogenizer [59,60]. The TEMPO-oxidized cellulose nanofibers (TOCNs) have homogenous ~3 nm width and are highly transparent (Figure 1.8).



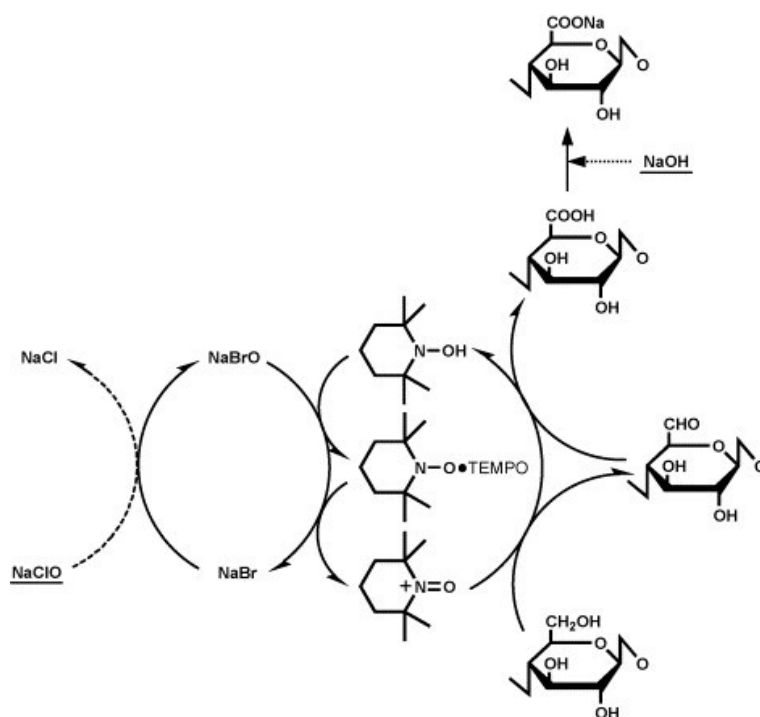


**Figure 1.7.** Selective oxidation of C6 primary hydroxyl groups to carboxylates by the TEMPO/NaBr/NaClO system in water under alkaline conditions. [55]

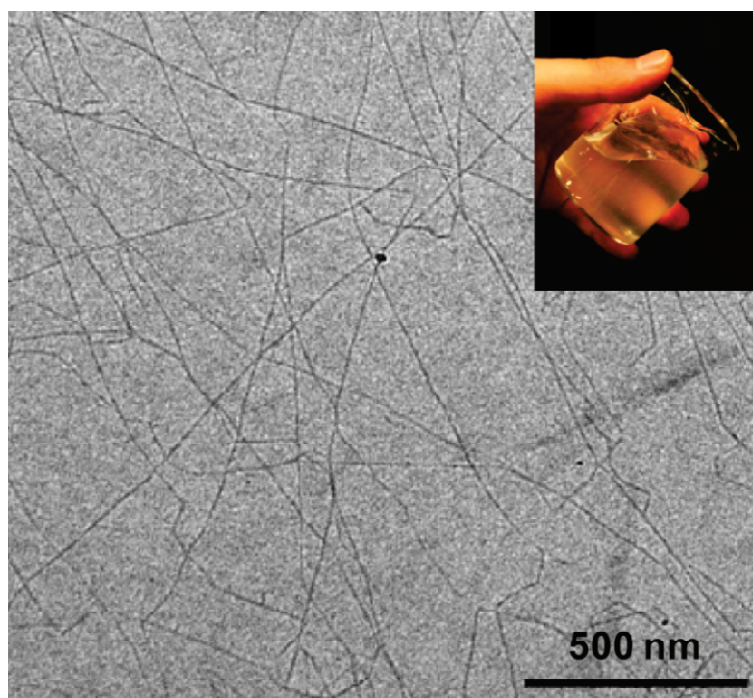


**Figure 1.8.** TEM image of TOCNs and the corresponding highly viscous and transparent dispersion. [60]

## 1.2 CNF-based composites

In nature, composite materials are constructed to be used for load-bearing, such as woods and bones. The cell walls of xylem are analogous to reinforced concrete, in which the micelle series of cellulose act similar as iron rods and the lignin together with hemicelluloses are the concrete [61]. The high stiffness and strength of cellulose crystals, as well as network structures of the microfibrils, make CNF an ideal candidate as reinforcements in polymers [62]. CNFs can be utilized in composites not just for reinforcements. In recent years, various kinds of block materials prepared of CNFs, such as self-standing films [63], hydrogels [64], aerogels [65], and foams [66], have been developed. These CNF materials showed some unique properties, such as high transmittance, excellent mechanical properties, gas-barrier properties, low thermal expansion, good biocompatibility and biodegradability [3]. Therefore, CNFs are also considered a promising matrix material to fabricate sustainable and functional composites.

### 1.2.1 CNF reinforced polymer composites

The dominant reason for exploiting nanocellulose in load-bearing composites is the potential to exploit the theoretically predicted stiffness and strength of cellulose crystals [62]. Theoretical estimations of the axial modulus of a cellulose crystal gave the value of 58-180 GPa, and tensile strength range from 0.3 to 22 GPa [62,67]. By far, Raman spectroscopy and X-ray diffraction results verified the tensile modulus of a single CNF varied between 100 and 160 GPa [13,68,69], and tensile strength measured by sonication ranged from 1.6 to 3.0 GPa [12].

Numerous polymer composites reinforced by CNFs were investigated [70–74]. The mechanical performances of some CNF reinforced polymer nanocomposites exceed the benchmark Poly-L-lactic acid (PLLA) when the volume of fraction of CNFs even < 10% [62], such as PLLA [75], regenerated cellulose [76], enzymatically modified rye arabinoxylan [77], and polyvinyl alcohol [78]. To obtain nanocomposites with higher mechanical performances reinforced by CNF, improving the efficiency of single-fiber level distribution in polymer matrix, making interfaces between CNFs and polymers with higher affinity, and establishing networks of CNFs are effective ways to achieve the goal [62]. In brief, nanocellulose is an excellent reinforcement for polymers. Using as reinforcements of polymer composites is considered a major application direction of CNFs.

### 1.2.2 Functional composites of inorganic/CNF

Natural materials are expected to replace most fossil energy materials. A significant intention of developing CNFs is based on their sustainability and environmental friendliness to the environment. In composite materials, the matrix material is the main component occupies most of the composite volume. Therefore, fabricating bulk materials of CNFs or exploiting them as matrix materials in making composites is more consistent with the concept of “green” material.

Organic/inorganic nanocomposites have been extensively studied to effectively impart the properties of inorganic materials, such as thermal stability, flame retardancy, mechanical properties, and gas barrier properties to polymer matrices [79–81]. When CNFs are combined with inorganic nanofillers, such as nanoclays [82], carbon nanotubes [83], and zinc oxide (ZnO) nanoparticles [84,85], the resulting nanofiller/TOCN composite films can display unique mechanical, optical, thermal, electrical, and oxygen barrier properties. For example, carbon nanotube/CNF composite films [83] are ultrastrong, transparent and exhibited good electrical conductivity, making them a promising wearable electrical material to realize green and flexible electronics. Different from using CNFs as reinforcements in polymers that aims at improving the mechanical performances of polymer matrix, the purpose of making composites with CNF-matrix is introducing the advantages of fillers to improve the properties of CNF materials and even give them new functional performances.

## 1.3 Zinc oxide/nanocellulose composites

### 1.3.1 Zinc oxide

ZnO is one of the most widely used inorganic additives to polymer matrices in the preparation of organic/inorganic nanocomposites because ZnO nanomaterials have unique physical and chemical properties such as fluorescence emission [86], piezoelectricity [87], UV absorption and scattering [88–90], photocatalytic activity [91], and antimicrobial activity [92]. ZnO nanomaterials, especially ZnO nanoparticles, are therefore widely used in synthetic rubbers, paints, flame retardants, solar cells, and medical applications.



### 1.3.2 Preparation of zinc oxide/nanocellulose nanocomposites

Methods of preparing ZnO/nanocellulose composites can be roughly divided into two categories: in situ ZnO nanoparticle formation through hydrolysis of zinc alkoxides in the presence of nanocellulose [93–95], and mechanical mixing of ZnO nanoparticles in aqueous nanocellulose dispersions [96,97].

Nanocelluloses have a high capacity to absorb metallic cations due to abundant hydroxyl groups or anionic groups presented on surfaces. The mechanism of *in-situ* preparation of ZnO nanoparticles on nanocelluloses was illustrated in Figure 1.9 [95]. In a typical procedure [98], ZnO/nanocelluloses composites were synthesized by first suspending the nanocellulose in water, then mixing with zinc salts (normally zinc acetate, zinc nitrate or zinc chloride) by magnetic stirring to have zinc ions absorbed on cellulose surfaces. After complete mixing, an alkali solution (sodium hydroxide or ammonium hydroxide) was dropwise added to the solution with continuous stirring at ~80 °C to form zinc hydroxide precipitates. After washing and separation, obtained products need to undergo oven drying at 120 °C for complete transformation of the remaining zinc hydroxide to ZnO. This method can prevent nanoparticle aggregation and improve dispersion, but the heat treatment at 120 °C is inevitable and the in situ preparation of ZnO/nanocellulose composites was reported to give a broad size distribution of ZnO particles [95]. In contrast, commercial ZnO nanoparticles have narrow size distributions. Moreover, it is more easily to have more diverse species of ZnO nanomaterials in other well-established systems that do not contain nanocellulose. Therefore, mechanical mixing of prepared ZnO nanoparticles with aqueous nanocellulose dispersions is more simple, universal and flexible, and thus promising, if ZnO particles can be homogeneously distributed in the nanocellulose matrix.

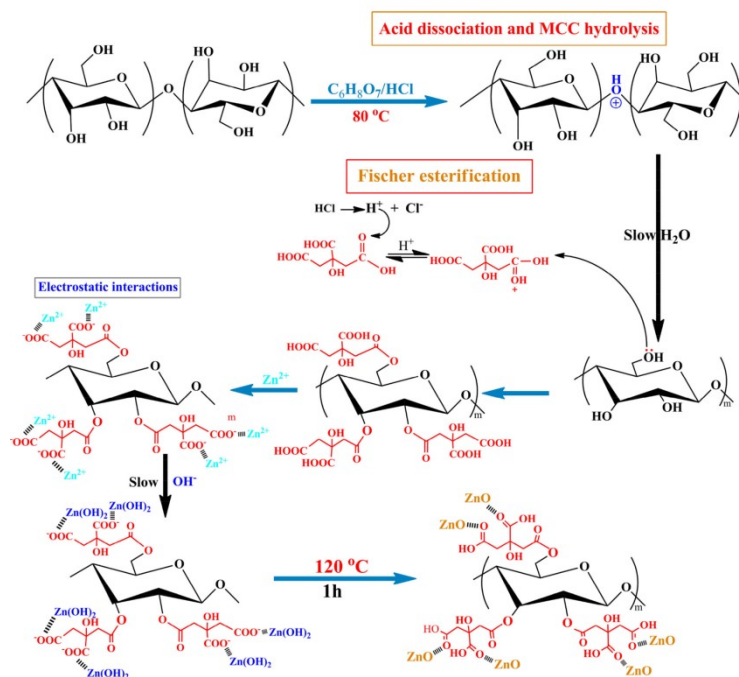


**Figure 1.9.** Schematic of CNC/ZnO nanohybrid fabrication. [95]

### 1.3.3 Multiple functions of zinc oxide/nanocellulose composites

#### *UV shielding*

ZnO is said to have the broadest UV spectrum absorption has broad UV absorption spectra among many inorganic and organic UV absorbers (Figure 1.10) [99]. Besides, ZnO is very stable under UV irradiation while the majority of the organic absorbers are ultimately destroyed by the UV radiation they absorb and gradually lost their UV-absorption efficiency. Therefore, ZnO is a very good UV absorber to make UV-shielding materials. Composites containing ZnO nanoparticles generally possess good UV-shielding properties, which is also true of ZnO/nanocellulose composites [100–102]. In particular, ZnO/CNC composite films prepared by casting and drying are high transparent but also with strong UV-blocking properties [96].

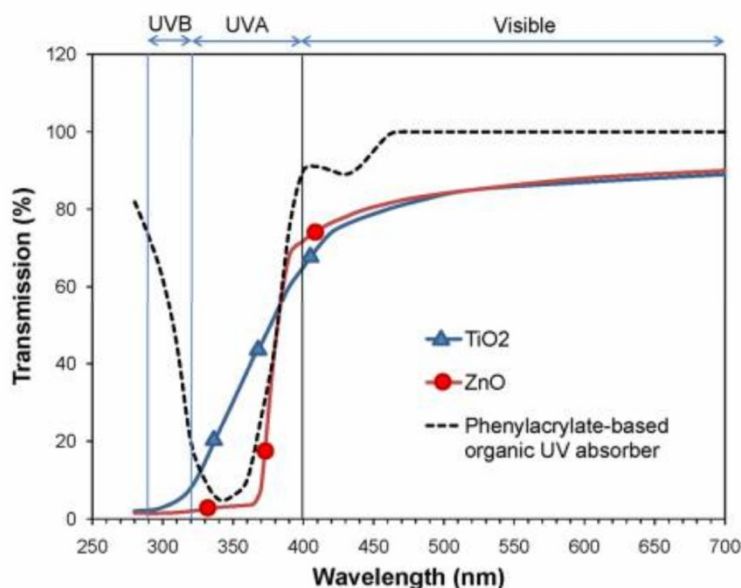


**Figure 1.10.** Typical transmission spectra of titanium dioxide (TiO<sub>2</sub>) nanoparticle suspensions, ZnO nanoparticle suspensions, and phenylacrylate-based organic absorber solutions. [99]

#### *Anti-microbial activity*

ZnO nanoparticles have a wide range of antibacterial activities toward various microorganisms that are commonly found in environmental settings, mainly due to the generation of reactive oxygen species and zinc ions release [103,104]. Moreover, the antibacterial activity did not require specific UV activation using artificial lamps, rather activation was achieved under ambient lighting conditions [103]. Highly effective antibacterial performances of ZnO/nanocellulose composites have been widely reported [97,104,105]. For instance, composites of NFC and ZnO nanoparticles are regarded as ideal antibacterial papers since they have shown bacteriostatic and/or bactericidal activity against both Gram positive and Gram negative bacteria [97].

#### *Photocatalytic activity*

ZnO, with a wide band gap (3.37 eV) and large exciton binding energy (60 meV), is one of the most popular n-type semiconductor metal oxides [106]. When irradiated by the light of energy higher or equal to the band gap energy, an electron from the valence band (VB) would be excited to the conduction band (CB) with simultaneous generation of a hole (h<sup>+</sup>) in the VB. The electron in CB and the hole in VB can recombine on the surface or in the bulk of the particle in a few nanoseconds, or can be separated under the built-in electric field to transfer to different positions on the surfaces to react

with donor or acceptor species adsorbed on or close to the surfaces. As a consequence, subsequent anodic and cathodic redox reactions can be initiated [107]. The photocatalytic activity of ZnO nanocrystals is influenced by the ZnO morphology, crystallization, and principally oxygen defects [108–110]. Making use of the photocatalytic activity of ZnO nanomaterials, several ZnO/cellulose nanocomposites were synthesized to achieve photodegradation of organic compounds [15,84,111,112].

#### *Thermal decomposition resistance*

Thermal degradation of cellulose involved depolymerization, dehydration, and decomposition of glycosyl units followed by formation of a charred residue [113]. The function of introducing ZnO to cellulose on thermal stability of the composite is disputable [114]. CNC/ZnO nanohybrids have better thermal stability than neat CNC [95,96,113], which was ascribed to the stronger interactions between oxygen atoms of the CNCs and ZnO nanoparticles, thus providing a thermal barrier for the cellulose skeleton by absorbing the heat [95,113]. However, some studies also showed that ZnO has no apparent influence on thermal stability or even reduce that of the cellulose [85,115,116]. ZnO reduced thermal stability is likely because of the high thermal conductivity of ZnO. Cellulose has low thermal conductivity, however, the direct interaction of ZnO and cellulose make heat transportation much easier which resulted in the lower thermal decomposition temperature.

#### *Multisource energy conversion*

Both mechanical and thermal energy can be harvested using piezoelectric materials. ZnO is a unique material of low cost that has both semiconductor and piezoelectric properties [117]. Energy transformation devices fabricated with ZnO nanostructures have achieved great progress [118]. Cellulose is a very suitable platform with good flexibility to fabricate energy-harvesting devices. Kumar et al. succeed in synthesizing ZnO nanostructure-embedded paper and using it for flexible strain-sensing devices [119]. By increasing ZnO density on one side of the ZnO/cellulose nanocomposite paper, they further demonstrated that this nanocomposite film can be directly used as energy-conversion devices to transform mechanical and thermal energies to electric power [120]. These mechanically robust and flexible devices can be fabricated over large areas and are capable of producing an output voltage and power up to 80 mV and 50 nW cm<sup>-2</sup>. Moreover, through integrating a certain number of the devices, significantly higher output voltage and output power can be achieved.

### *Water repellency*

Cellulose is a highly hydrophilic and hygroscopic material by nature due to the hydroxyl groups of glucose monomers. For cellulose crystals, they have an amphiphilic nature. Uneven exposure of chemical functions on the crystal faces resulting in hydrophobic or hydrophilic character of the faces [121]. The (100) crystalline plane of nanocelluloses have a surface covered by a rich layer of CH methine groups and thus hydrophobic [122]. But overall, nanocelluloses are generally very hydrophilic, particularly for nanocelluloses like TOCNs that abundant hydrophilic groups (e.g. carboxylate groups) have been introduced to their surfaces. The high hydrophilicity could lead to performance deteriorations of some properties of nanocellulose materials, such as oxygen permeability. Production of hydrophobic surfaces can be achieved by making a rough surface and modifying the surface with material of low surface energy [123]. Many superhydrophobic coating on cellulose-based materials have been developed, such as dip-coating, spray-coating, polymerization techniques, *in site* nanorod or particle growth, and so on [124]. Both ZnO coated nanocellulose by covalent deposition and composite films of ZnO/nanocellulose prepared by mechanical mixing exhibited the transformation from superhydrophilic to superhydrophobic [96,125,126] (Figure 1.11), through the generation of rough surfaces.

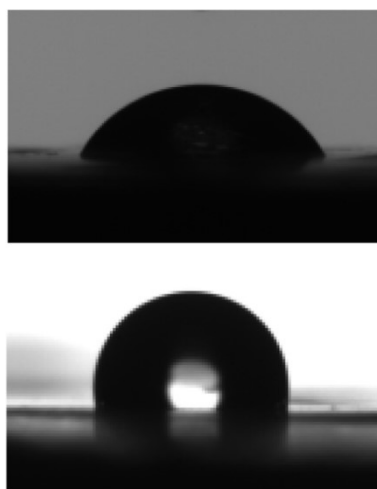


**Figure 1.11.** Representative images of a water drop at the surface of (upper image) neat CNC and (under image) ZnO/CNC composite film (ZnO content is 5 wt.%) prepared by mechanical mixing. [96]

On the other hand, some photoactive inorganic materials, such as ZnO and titanium dioxide (TiO<sub>2</sub>) coated cellulose materials also show photo-switchable wetting properties [127]. The (001) plane of the

ZnO nanorod films has low surface energy and leads to a superhydrophobic surface of the ZnO film. However, when being exposed to UV radiation, electron-hole pairs would generate and result in the adsorption of hydroxyl group on the ZnO surface. Consequently, the superhydrophobic property of ZnO nanorod film is converted to superhydrophilic. Storage in dark can made the film revert to superhydrophobic [128]. Therefore, ZnO/nanocellulose nanocomposites could also have interesting photo-induced wettability switching.

## 1.4 Research objectives

This study aims at preparing uniform ZnO/TOCN composite films by simple mechanical mixing and investigating the film properties when different amounts or morphologies of ZnO nanoparticles are used. Multiple functions of the prepared nanocomposite films were characterized and studied, including optical, mechanical, thermal, hydrophilic, anti-microbial properties, as well as photocatalytic activity and oxygen permeability. Besides of this, two related subjects developed during the study of ZnO/TOCN nanocomposites, UV-induced degradation of TOCNs in water dispersions and influence of counter-ions of surface carboxylates of TOCNs on cell viability were also involved in this thesis.

In chapter 2, uniform ZnO/TOCN nanocomposite films were successfully prepared by a simple mechanical mixing method. Influences of the adding amount of ZnO nanoparticles on light-transmittance and UV-shielding, thermal stability, surface wettability, mechanical properties, and anti-microbial performance were investigated.

In chapter 3, ZnO nanoparticles with different morphologies were used in preparing ZnO/TOCN composite films and influences of the morphology of ZnO nanoparticles on the nanocomposite films were investigated. Thermal, mechanical properties (elastic modulus and tensile strength) and surface wettability of composite films were characterized but no apparent change was observed when applying ZnO nanoparticles with different diameter and aspect ratios. Optical properties (transmittance, UV shielding, and photoluminescence [PL]), X-ray diffraction (XRD) results, photocatalytic activity, and oxygen permeability were mainly exhibited and discussed in this chapter.

In chapter 4, UV-induced degradation of TOCNs in water dispersion was studied. Many changes took place in TOCNs during the UV irradiation. Changes in viscosity, transmittance, pH value, ratio of

water-insoluble fractions of TOCN dispersions depend on different irradiation times were determined. Beyond that, many changes occurred on the nanofibers, such as width and length, molecular weight, functional groups, and crystals of TOCNs with different length and surface carboxylate contents, as well as analysis of the water-soluble fraction after UV were also investigated.

In chapter 5, TOCNs with different lengths and carboxylate contents and counter-ions of surface carboxylates were fabricated to investigate the influence of ions of CNF surfaces on cellular biocompatibility. In this chapter, cellular biocompatibility of TOCNs prepared under different TEMPO-mediated oxidation conditions were studied by determining the overall cell viability, cell population analysis and intracellular changes of intracellular reactive oxygen species (ROS) and mitochondrial changes. The influence of carboxylate contents and nanofibrils lengths, as well as counter-ions was discussed.

Chapter 6 is a summary of the whole thesis.

## 1.5 References

- [1] J.H. Kim, B.S. Shim, H.S. Kim, Y.J. Lee, S.K. Min, D. Jang, Z. Abas, J. Kim, Review of nanocellulose for sustainable future materials, *Int. J. Precis. Eng. Manuf. - Green Technol.* 2 (2015) 197–213.
- [2] A. Isogai, Wood nanocelluloses: fundamentals and applications as new bio-based nanomaterials, *J. Wood Sci.* 59 (2013) 449–459.
- [3] A. Isogai, T. Saito, H. Fukuzumi, TEMPO-oxidized cellulose nanofibers, *Nanoscale.* 3 (2011) 71–85.
- [4] M.S. Doblin, I. Kurek, D. Jacob-Wilk, D.P. Delmer, Cellulose biosynthesis in plants: From genes to rosettes, *Plant Cell Physiol.* 43 (2002) 1407–1420.
- [5] E. Slabaugh, J.K. Davis, C.H. Haigler, Y.G. Yingling, J. Zimmer, Cellulose synthases: New insights from crystallography and modeling, *Trends Plant Sci.* 19 (2014) 99–106.
- [6] N.G. Taylor, Cellulose biosynthesis and deposition in higher plants, *New Phytol.* 178 (2008) 239–252.
- [7] A. Ishikawa, T. Okano, J. Sugiyama, Fine structure and tensile properties of ramie fibres in the crystalline form of cellulose I, II, III and IV, *Polymer (Guildf).* 38 (1997) 463–468.
- [8] T. Nishino, K. Takano, K. Nakamae, Elastic modulus of the crystalline regions of cellulose polymorphs, *J. Polym. Sci. Part B Polym. Phys.* 33 (1995) 1647–1651.
- [9] K.H. Gardivert, J. Blackwell, The structure of native Cellulose, *Biopolymers.* 13 (2001) 1975–2001.
- [10] Y. Nishiyama, Structure and properties of the cellulose microfibril, *J. Wood Sci.* 55 (2009) 241–249.
- [11] S. Iwamoto, W. Kai, A. Isogai, T. Iwata, Elastic modulus of single cellulose microfibrils from tunicate measured by atomic force microscopy, *Biomacromolecules.* 10 (2009) 2571–2576.

- [12] T. Saito, R. Kuramae, J. Wohler, L.A. Berglund, A. Isogai, An ultrastrong nanofibrillar biomaterial: The strength of single cellulose nanofibrils revealed via sonication-induced fragmentation, *Biomacromolecules*. 14 (2013) 248–253.
- [13] I. Sakurada, Y. Nukushina, T. Ito, Experimental determination of the elastic modulus of crystalline regions in oriented polymers, *J. Polym. Sci.* 57 (1962) 651–660.
- [14] S. Masaoka, T. Ohe, N. Sakota, Production of cellulose from glucose by *Acetobacter xylinum*, *J. Ferment. Bioeng.* 75 (1993) 18–22.
- [15] M. Iguchi, S. Yamanaka, A. Budhiono, Bacterial cellulose—a masterpiece of nature’s arts, *J. Mater. Sci.* 35 (2000) 261–270.
- [16] D. Klemm, B. Heublein, H.P. Fink, A. Bohn, Cellulose: Fascinating biopolymer and sustainable raw material, *Angew. Chem. Int. Ed.* 44 (2005) 3358–3393.
- [17] D. Klemm, D. Schumann, U. Udhardt, S. Marsch, Bacterial synthesized cellulose—artificial blood vessels for microsurgery, *Prog. Polym. Sci.* 26 (2001) 1561–1603.
- [18] M. Martínez-Sanz, A. Lopez-Rubio, J.M. Lagaron, Optimization of the nanofabrication by acid hydrolysis of bacterial cellulose nanowhiskers, *Carbohydr. Polym.* 85 (2011) 228–236.
- [19] S. Yamanaka, M. Ishihara, J. Sugiyama, Structural modification of bacterial cellulose, *Cellulose*. 7 (2000) 213–225.
- [20] I. Siró, D. Plackett, Microfibrillated cellulose and new nanocomposite materials: A review, *Cellulose*. 17 (2010) 459–494.
- [21] W. Czaja, D. Romanovicz, R. malcolm Brown, Structural investigations of microbial cellulose produced in stationary and agitated culture, *Cellulose*. 11 (2004) 403–411.
- [22] S. Park, J.O. Baker, M.E. Himmel, P.A. Parilla, D.K. Johnson, Cellulose crystallinity index: Measurement techniques and their impact on interpreting cellulase performance, *Biotechnol. Biofuels*. 3 (2010) 1–10.
- [23] D.N.S. Hon, Cellulose: a random walk along its historical path, *Cellulose*. 1 (1994) 1–25.
- [24] K. Wickholm, P.T. Larsson, T. Iversen, Assignment of non-crystalline forms in cellulose I by CP/MAS <sup>13</sup>C NMR spectroscopy, *Carbohydr. Res.* 312 (1998) 123–129.
- [25] H. Zhao, J.H. Kwak, Z. Conrad Zhang, H.M. Brown, B.W. Arey, J.E. Holladay, Studying cellulose fiber structure by SEM, XRD, NMR and acid hydrolysis, *Carbohydr. Polym.* 68 (2007) 235–241.
- [26] Y. Nishiyama, U.J. Kim, D.Y. Kim, K.S. Katsumata, R.P. May, P. Langan, Periodic disorder along ramie cellulose microfibrils, *Biomacromolecules*. 4 (2003) 1013–1017.
- [27] B.B. Hallac, A.J. Ragauskas, Analyzing cellulose degree of polymerization and its relevancy to cellulosic ethanol, *Biofuels, Bioprod. Biorefining*. 5 (2011) 215–225. doi:10.1002/bbb.
- [28] O.A. Battista, Hydrolysis and crystallization of cellulose, *Ind. Eng. Chem.* 42 (1950) 502–507.
- [29] X.M. Dong, J.F. Revol, D.G. Gray, Effect of microcrystallite preparation conditions on the formation of colloid crystals of cellulose, *Cellulose*. 5 (1998) 19–32.
- [30] B. Sun, M. Zhang, Q. Hou, R. Liu, T. Wu, C. Si, Further characterization of cellulose nanocrystal (CNC) preparation from sulfuric acid hydrolysis of cotton fibers, *Cellulose*. 23 (2016) 439–450.
- [31] R.J. Moon, A. Martini, J. Nairn, J. Simonsen, J. Youngblood, Cellulose nanomaterials review: Structure, properties and nanocomposites, *Chem. Soc. Rev.* 40 (2011) 3941–3994.
- [32] J. Araki, M. Wada, S. Kuga, T. Okano, Influence of surface charge on viscosity behavior of cellulose microcrystal suspension, *J. Wood Sci.* 45 (1999) 258–261.



- [33] L. Chen, Q. Wang, K. Hirth, C. Baez, U.P. Agarwal, J.Y. Zhu, Tailoring the yield and characteristics of wood cellulose nanocrystals (CNC) using concentrated acid hydrolysis, *Cellulose*. 22 (2015) 1753–1762.
- [34] Q. Wang, X. Zhao, J.Y. Zhu, Kinetics of strong acid hydrolysis of a bleached kraft pulp for producing cellulose nanocrystals (CNCs), *Ind. Eng. Chem. Res.* 53 (2014) 11007–11014.
- [35] S. Elazzouzi-Hafraoui, Y. Nishiyama, J.L. Putaux, L. Heux, F. Dubreuil, C. Rochas, The shape and size distribution of crystalline nanoparticles prepared by acid hydrolysis of native cellulose, *Biomacromolecules*. 9 (2008) 57–65.
- [36] P. Lu, Y. Lo Hsieh, Preparation and characterization of cellulose nanocrystals from rice straw, *Carbohydr. Polym.* 87 (2012) 564–573.
- [37] O. van der Berg, J.R. Capadona, C. Weder, Preparation of homogeneous dispersions of tunicate cellulose whiskers in organic solvents, *Biomacromolecules*. 8 (2007) 1353–1357.
- [38] S. Camarero Espinosa, T. Kuhnt, E.J. Foster, C. Weder, Isolation of thermally stable cellulose nanocrystals by phosphoric acid hydrolysis, *Biomacromolecules*. 14 (2013) 1223–1230.
- [39] N. Mahfoudhi, S. Boufi, Nanocellulose as a novel nanostructured adsorbent for environmental remediation: a review, *Cellulose*. 24 (2017) 1171–1197.
- [40] H.P.S.A. Khalil, A.H. Bhat, A.F.I. Yusra, Green composites from sustainable cellulose nanofibrils: A review, *Carbohydr. Polym.* 87 (2012) 963–979.
- [41] A.F. Turbak, F.W. Snyder, K.R. Sandberg, Microfibrillated cellulose, a new cellulose product: Properties, uses, and commercial potential, *J. Appl. Polym. Sci. Appl. Polym. Symp.* 37 (1983) 815–827.
- [42] F.W. Herrick, R.L. Casebier, J.K. Hamilton, K.R. Sandberg, Microfibrillated cellulose: Morphology and accessibility, *J. Appl. Polym. Sci. Appl. Polym. Symp.* 37 (1983) 797–813.
- [43] W. Stelte, A.R. Sanadi, Preparation and characterization of cellulose nanofibers from two commercial hardwood and softwood pulps, *Ind. Eng. Chem. Res.* 48 (2009) 11211–11219.
- [44] S. Iwamoto, K. Abe, H. Yano, The effect of hemicelluloses on wood pulp nanofibrillation and nanofiber network characteristics, *Biomacromolecules*. 9 (2008) 1022–1026.
- [45] T. Zimmermann, N. Bordeanu, E. Strub, Properties of nanofibrillated cellulose from different raw materials and its reinforcement potential, *Carbohydr. Polym.* 79 (2010) 1086–1093.
- [46] Ø. Eriksen, K. Syverud, Ø. Gregersen, The use of microfibrillated cellulose produced from kraft pulp as strength enhancer in TMP paper, *Nord. Pulp Pap. Res. J.* 23 (2008) 299–304.
- [47] M. Ankerfors, T. Lindström, On the manufacture and use of nanocellulose, in: 9th Int. Conf. Wood Biofiber Plast. Compos., May. 2007.
- [48] M. Pääkko, M. Ankerfors, H. Kosonen, A. Nykänen, S. Ahola, M. Österberg, J. Ruokolainen, J. Laine, P.T. Larsson, O. Ikkala, T. Lindström, Enzymatic hydrolysis combined with mechanical shearing and high-pressure homogenization for nanoscale cellulose fibrils and strong gels, *Biomacromolecules*. 8 (2007) 1934–1941.
- [49] M. Henriksson, G. Henriksson, L.A. Berglund, T. Lindström, An environmentally friendly method for enzyme-assisted preparation of microfibrillated cellulose (MFC) nanofibers, *Eur. Polym. J.* 43 (2007) 3434–3441.
- [50] N. Hayashi, T. Kondo, M. Ishihara, Enzymatically produced nano-ordered short elements containing cellulose I $\beta$  crystalline domains, *Carbohydr. Polym.* 61 (2005) 191–197.
- [51] H. Liimatainen, M. Visanko, J.A. Sirviö, O.E.O. Hormi, J. Niinimäki, Enhancement of the nanofibrillation of wood cellulose through sequential periodate-chlorite oxidation,

- Biomacromolecules. 13 (2012) 1592–1597.
- [52] T. Saito, Y. Nishiyama, J.L. Putaux, M. Vignon, A. Isogai, Homogeneous suspensions of individualized microfibrils from TEMPO-catalyzed oxidation of native cellulose, *Biomacromolecules*. 7 (2006) 1687–1691.
  - [53] A.E.J. de Nooy, A.C. Besemer, H. van Bekkum, Highly selective nitroxyl radical-mediated oxidation of primary alcohol groups in water-soluble glucans, *Carbohydr. Res.* 269 (1995) 89–98.
  - [54] T. Isogai, M. Yanagisawa, A. Isogai, Degrees of polymerization (DP) and DP distribution of cellouronic acids prepared from alkali-treated celluloses and ball-milled native celluloses by TEMPO-mediated oxidation, *Cellulose*. 16 (2009) 117–127.
  - [55] T. Saito, A. Isogai, Introduction of aldehyde groups on surfaces of native cellulose fibers by TEMPO-mediated oxidation, *Colloids Surfaces A Physicochem. Eng. Asp.* 289 (2006) 219–225.
  - [56] W.F. Bailey, J.M. Bobbitt, K.B. Wiberg, Mechanism of the oxidation of alcohols by oxoammonium cations, *J. Org. Chem.* 72 (2007) 4504–4509.
  - [57] S. Goldstein, A. Samuni, Kinetics and mechanism of peroxy radical reactions with nitroxides, *J. Phys. Chem. A*. 111 (2007) 1066–1072.
  - [58] T. Saito, A. Isogai, TEMPO-mediated oxidation of native cellulose. The effect of oxidation conditions on chemical and crystal structures of the water-insoluble fractions, *Biomacromolecules*. 5 (2004) 1983–1989.
  - [59] T. Saito, S. Kimura, Y. Nishiyama, A. Isogai, Cellulose nanofibers prepared by TEMPO-mediated oxidation of native cellulose, *Biomacromolecules*. 8 (2007) 2485–2491.
  - [60] T. Saito, M. Hirota, N. Tamura, S. Kimura, H. Fukuzumi, L. Heux, A. Isogai, Individualization of nano-sized plant cellulose fibrils achieved by direct surface carboxylation using TEMPO catalyst, (2009) 1992–1996.
  - [61] K. Freudenberg, The relationship of cellulose to lignin in wood, *J. Chem. Educ.* 9 (1932) 1171–1180.
  - [62] K.Y. Lee, Y. Aitomäki, L.A. Berglund, K. Oksman, A. Bismarck, On the use of nanocellulose as reinforcement in polymer matrix composites, *Compos. Sci. Technol.* 105 (2014) 15–27.
  - [63] H. Fukuzumi, T. Saito, T. Wata, Y. Kumamoto, A. Isogai, Transparent and high gas barrier films of cellulose nanofibers prepared by TEMPO-mediated oxidation, *Biomacromolecules*. 10 (2009) 162–165.
  - [64] T. Saito, T. Uematsu, S. Kimura, T. Enomae, A. Isogai, Self-aligned integration of native cellulose nanofibrils towards producing diverse bulk materials, *Soft Matter*. 7 (2011) 8804–8809.
  - [65] Y. Kobayashi, T. Saito, A. Isogai, Aerogels with 3D ordered nanofiber skeletons of liquid-crystalline nanocellulose derivatives as tough and transparent insulators, *Angew. Chem. Int. Ed. Engl.* 53 (2014) 10394–10397.
  - [66] P. Munier, K. Gordeyeva, L. Bergström, A.B. Fall, Directional freezing of nanocellulose dispersions aligns the rod-like particles and produces low-density and robust particle networks, *Biomacromolecules*. 17 (2016) 1875–1881.
  - [67] M. Ioelovich, Cellulose as a nanostructured polymer: A short review, *BioResources*. 3 (2008) 1403–1418.
  - [68] M. Matsuo, C. Sawatari, Y. Iwai, F. Ozaki, Effect of orientation distribution and crystallinity

- on the measurement by x-ray diffraction of the crystal lattice moduli of cellulose I and II, *Macromolecules*. 23 (1990) 3266–3275.
- [69] A. Štuncová, G.R. Davies, S.J. Eichhorn, Elastic modulus and stress-transfer properties of tunicate cellulose whiskers, *Biomacromolecules*. 6 (2005) 1055–1061.
- [70] H. Soeta, S. Fujisawa, T. Saito, L. Berglund, A. Isogai, Low-birefringent and highly tough nanocellulose-reinforced cellulose triacetate, *ACS Appl. Mater. Interfaces*. 7 (2015) 11041–11046.
- [71] S. Fujisawa, T. Saito, S. Kimura, T. Iwata, A. Isogai, Comparison of mechanical reinforcement effects of surface-modified cellulose nanofibrils and carbon nanotubes in PLLA composites, *Compos. Sci. Technol.* 90 (2014) 96–101.
- [72] V. Favier, H. Chanzy, J.Y. Cavaillé, Polymer Nanocomposites Reinforced by Cellulose Whiskers, *Macromolecules*. 28 (1995) 6365–6367.
- [73] V. Favier, G.R. Canova, J.Y. Cavaillé, H. Chanzy, A. Dufresne, C. Gauthier, Nanocomposite materials from latex and cellulose whiskers, *Polym. Adv. Technol.* 6 (1995) 351–355.
- [74] A. Boldizar, C. Klason, J. Kubát, P. Näslund, P. Sáha, Prehydrolyzed cellulose as reinforcing filler for thermoplastics, *Int. J. Polym. Mater. Polym. Biomater.* 11 (1987) 229–262.
- [75] M. Jonoobi, J. Harun, A.P. Mathew, K. Oksman, Mechanical properties of cellulose nanofiber (CNF) reinforced polylactic acid (PLA) prepared by twin screw extrusion, *Compos. Sci. Technol.* 70 (2010) 1742–1747.
- [76] T. Pullawan, A.N. Wilkinson, S.J. Eichhorn, Discrimination of matrix-fibre interactions in all-cellulose nanocomposites, *Compos. Sci. Technol.* 70 (2010) 2325–2330.
- [77] K.S. Mikkonen, L. Pitkänen, V. Liljeström, E. Mabasa Bergström, R. Serimaa, L. Salmén, M. Tenkanen, Arabinoxylan structure affects the reinforcement of films by microfibrillated cellulose, *Cellulose*. 19 (2012) 467–480.
- [78] J. Lu, T. Wang, L.T. Drzal, Preparation and properties of microfibrillated cellulose polyvinyl alcohol composite materials, *Compos. Part A Appl. Sci. Manuf.* 39 (2008) 738–746.
- [79] J.W. Gilman, Flammability and thermal stability studies of polymer layered-silicate (clay) nanocomposites, *Appl. Clay Sci.* 15 (1999) 31–49.
- [80] W. Tang, M.H. Santare, S.G. Advani, Melt processing and mechanical property characterization of multi-walled carbon nanotube/high density polyethylene (MWNT/HDPE) composite films, *Carbon*. 41 (2003) 2779–2785.
- [81] X. Ma, P.R. Chang, J. Yang, J. Yu, Preparation and properties of glycerol plasticized-pea starch/zinc oxide-starch bionanocomposites, *Carbohydr. Polym.* 75 (2009) 472–478.
- [82] C.N. Wu, T. Saito, S. Fujisawa, H. Fukuzumi, A. Isogai, Ultrastrong and high gas-barrier nanocellulose/clay-layered composites, *Biomacromolecules*. 13 (2012) 1927–1932.
- [83] H. Koga, T. Saito, T. Kitaoka, M. Nogi, K. Suganuma, A. Isogai, Transparent, conductive, and printable composites consisting of TEMPO-oxidized nanocellulose and carbon nanotube, *Biomacromolecules*. 14 (2013) 1160–1165. doi:10.1021/bm400075f.
- [84] R. Ning, M. Takeuchi, J.M. Lin, T. Saito, A. Isogai, Influence of the morphology of zinc oxide nanoparticles on the properties of zinc oxide/nanocellulose composite films, *React. Funct. Polym.* 131 (2018) 293–298.
- [85] R. Ning, C.N. Wu, M. Takeuchi, T. Saito, A. Isogai, Preparation and characterization of zinc oxide/TEMPO-oxidized cellulose nanofibril composite films, *Cellulose*. 24 (2017) 4861–4870.
- [86] H. Xiong, Y. Xu, Q. Ren, Y. Xia, Stable aqueous ZnO polymer core-shell nanoparticles with

- tunable photoluminescence and their application in cell imaging, *J. Am. Chem. Soc.* 130 (2008) 7522–7523.
- [87] Q. Yang, Y. Liu, C. Pan, J. Chen, X. Wen, Z.L. Wang, Largely enhanced efficiency in ZnO nanowire/p-polymer hybridized inorganic/organic ultraviolet light-emitting diode by piezo-phototronic effect, *Nano Lett.* 13 (2013) 607–613.
  - [88] O.M. El-Feky, E.A. Hassan, S.M. Fadel, M.L. Hassan, Use of ZnO nanoparticles for protecting oil paintings on paper support against dirt, fungal attack, and UV aging, *J. Cult. Herit.* 15 (2014) 165–172.
  - [89] Y.Q. Li, S.Y. Fu, Y.W. Mai, Preparation and characterization of transparent ZnO/epoxy nanocomposites with high-UV shielding efficiency, *Polymer (Guildf)*. 47 (2006) 2127–2132.
  - [90] M.M.A. El-Hady, A. Farouk, S. Sharaf, Flame retardancy and UV protection of cotton based fabrics using nano ZnO and polycarboxylic acids, *Carbohydr. Polym.* 92 (2013) 400–406.
  - [91] D. Chen, Z. Wang, T. Ren, H. Ding, W. Yao, R. Zong, Y. Zhu, Influence of defects on the photocatalytic activity of ZnO, *J. Phys. Chem. C*. 118 (2014) 15300–15307.
  - [92] S. Shankar, J.P. Reddy, J.W. Rhim, H.Y. Kim, Preparation, characterization, and antimicrobial activity of chitin nanofibrils reinforced carrageenan nanocomposite films, *Carbohydr. Polym.* 117 (2015) 468–475.
  - [93] M. Yadollahi, I. Gholamali, H. Namazi, M. Aghazadeh, Synthesis and characterization of antibacterial carboxymethyl cellulose/ZnO nanocomposite hydrogels, *Int. J. Biol. Macromol.* 74 (2015) 136–141.
  - [94] A. John, H.U. Ko, D.G. Kim, J. Kim, Preparation of cellulose-ZnO hybrid films by a wet chemical method and their characterization, *Cellulose*. 18 (2011) 675–680.
  - [95] H.Y. Yu, G.Y. Chen, Y.B. Wang, J.M. Yao, A facile one-pot route for preparing cellulose nanocrystal/zinc oxide nanohybrids with high antibacterial and photocatalytic activity, *Cellulose*. 22 (2015) 261–273.
  - [96] E. Lizundia, A. Urruchi, J.L. Vilas, L.M. Leon, Increased functional properties and thermal stability of flexible cellulose nanocrystal/ZnO films, *Carbohydr. Polym.* 136 (2016) 250–258.
  - [97] N.C.T. Martins, R. Freire, Carmen S, C.P. Neto, A.J.D. Silvestre, J. Causio, G. Baldi, P. Sadocco, T. Trindade, Antibacterial paper based on composite coatings of nanofibrillated cellulose and ZnO, *Colloids Surfaces A Physicochem. Eng. Asp.* 417 (2013) 111–119.
  - [98] S. Azizi, M. Ahmad, M. Mahdavi, S. Abdolmohammadi, Preparation, characterization, and antimicrobial activities of ZnO nanoparticles/cellulose nanocrystal nanocomposites, *BioResources*. 8 (2013) 1841–1851.
  - [99] T. Tsuzuki, X. Wang, Nanoparticle coatings for UV protective textiles, *Res. J. Text. Appar.* 14 (2010) 9 – 21.
  - [100] F. Grüneberger, T. Künniger, A. Huch, T. Zimmermann, M. Arnold, Nanofibrillated cellulose in wood coatings: Dispersion and stabilization of ZnO as UV absorber, *Prog. Org. Coatings*. 87 (2015) 112–121.
  - [101] A. Becheri, M. Dürr, P. Lo Nostro, P. Baglioni, Synthesis and characterization of zinc oxide nanoparticles: Application to textiles as UV-absorbers, *J. Nanoparticle Res.* 10 (2008) 679–689.
  - [102] Y. Li, Y. Zou, Y. Hou, Fabrication and UV-blocking property of nano-ZnO assembled cotton fibers via a two-step hydrothermal method, *Cellulose*. 18 (2011) 1643–1649.
  - [103] K.R. Raghupathi, R.T. Koodali, A.C. Manna, Size-dependent bacterial growth inhibition and

- mechanism of antibacterial activity of zinc oxide nanoparticles, *Langmuir*. 27 (2011) 4020–4028.
- [104] A. Sirelkhatim, S. Mahmud, A. Seenii, N.H.M. Kaus, L.C. Ann, S.K.M. Bakhori, H. Hasan, D. Mohamad, Review on zinc oxide nanoparticles: Antibacterial activity and toxicity mechanism, *Nano-Micro Lett.* 7 (2015) 219–242.
- [105] K. Lefatshe, C.M. Muiva, L.P. Kebaabetswe, Extraction of nanocellulose and in-situ casting of ZnO/cellulose nanocomposite with enhanced photocatalytic and antibacterial activity, *Carbohydr. Polym.* 164 (2017) 301–308.
- [106] Y. Zheng, C. Chen, Y. Zhan, X. Lin, Q. Zheng, K. Wei, J. Zhu, Y. Zhu, Luminescence and photocatalytic activity of ZnO nanocrystals: Correlation between structure and property, *Inorg. Chem.* 46 (2007) 6675–6682. doi:10.1021/ic062394m.
- [107] L. Jing, Y. Qu, B. Wang, S. Li, B. Jiang, L. Yang, W. Fu, H. Fu, J. Sun, Review of photoluminescence performance of nano-sized semiconductor materials and its relationships with photocatalytic activity, *Sol. Energy Mater. Sol. Cells*. 90 (2006) 1773–1787.
- [108] A. McLaren, T. Valdes-Solis, G. Li, C.T. Shik, Shape and size effects of ZnO nanocrystals on photocatalytic activity, *J. Am. Chem. Soc.* 131 (2009) 12540–12541.
- [109] J. Wang, Z. Wang, B. Huang, Y. Ma, Y. Liu, X. Qin, X. Zhang, Y. Dai, Oxygen vacancy induced band-gap narrowing and enhanced visible light photocatalytic activity of ZnO, *ACS Appl. Mater. Interfaces*. 4 (2012) 4024–4030.
- [110] E.S. Jang, J.H. Won, S.J. Hwang, J.H. Choy, Fine tuning of the face orientation of ZnO crystals to optimize their photocatalytic activity, *Adv. Mater.* 18 (2006) 3309–3312.
- [111] C. Luo, Y. Ma, H. Li, F. Chen, K. Uchiyama, J.M. Lin, Generation of picoliter droplets of liquid for electrospray ionization with piezoelectric inkjet, *J. Mass Spectrom.* 48 (2013) 321–328.
- [112] Q. He, C. Ma, X. Hu, H. Chen, Method for fabrication of paper-based microfluidic devices by alkylsilane self-assembling and UV/O<sub>3</sub>-patterning, *Anal. Chem.* 85 (2013) 1327–1331.
- [113] S. Azizi, M.B. Ahmad, M.Z. Hussein, N.A. Ibrahim, Synthesis, antibacterial and thermal studies of cellulose nanocrystal stabilized ZnO-Ag heterostructure nanoparticles, *Molecules*. 18 (2013) 6269–6280.
- [114] S.W. Zhao, C.R. Guo, Y.Z. Hu, Y.R. Guo, Q.J. Pan, The preparation and antibacterial activity cellulose/ZnO composite : a review, *Open Chem.* 16 (2018) 9–20.
- [115] D. Qin, Y. Xia, G.M. Whitesides, Soft lithography for micro- and nanoscale patterning., *Nat. Protoc.* 5 (2010) 491–502. doi:10.1038/nprot.2009.234.
- [116] M.B. Byrne, M.T. Lesile, H.R. Gaskins, P.J.A. Kenis, Methods to study the tumor microenvironment under controlled oxygen conditions, *Trends Biotechnol.* 32 (2014) 556–563.
- [117] Ü. Özgür, Y.I. Alivov, C. Liu, A. Teke, M.A. Reshchikov, S. Doğan, V. Avrutin, S.J. Cho, H. Morkoç, A comprehensive review of ZnO materials and devices, *J. Appl. Phys.* 98 (2005) 1–103.
- [118] Z.L. Wang, J. Song, Piezoelectric nanogenerators based on zinc oxide nanowire arrays, *Science*. 312 (2006) 242–246.
- [119] H. Gullapalli, V.S.M. Vemuru, A. Kumar, A. Botello-Mendez, R. Vajtai, M. Terrones, S. Nagarajaiah, P.M. Ajayan, Flexible piezoelectric zno-paper nanocomposite strain sensor, *Small*. 6 (2010) 1641–1646.
- [120] A. Kumar, H. Gullapalli, K. Balakrishnan, A. Botello-Mendez, R. Vajtai, M. Terrones, P.M.

- Ajayan, Flexible ZnO-cellulose nanocomposite for multisource energy conversion, *Small*. 7 (2011) 2173–2178.
- [121] C. Moreau, A. Villares, I. Capron, B. Cathala, Tuning supramolecular interactions of cellulose nanocrystals to design innovative functional materials, *Ind. Crops Prod.* 93 (2016) 96–107.
  - [122] I. Capron, O.J. Rojas, R. Bordes, Behavior of nanocelluloses at interfaces, *Curr. Opin. Colloid Interface Sci.* 29 (2017) 83–95.
  - [123] V.A. Ganesh, H.K. Raut, A.S. Nair, S. Ramakrishna, A review on self-cleaning coatings, *J. Mater. Chem.* 21 (2011) 16304–16322.
  - [124] H. Teisala, M. Tuominen, J. Kuusipalo, Superhydrophobic Coatings on Cellulose-Based Materials: Fabrication, Properties, and Applications, *Adv. Mater. Interfaces.* 1 (2014) 1–20.
  - [125] M. Zhang, D. Zang, J. Shi, Z. Gao, C. Wang, J. Li, Superhydrophobic cotton textile with robust composite film and flame retardancy, *RSC Adv.* 5 (2015) 67780–67786.
  - [126] R.H.A. Ras, X. Tian, I.S. Bayer, Superhydrophobic and Superoleophobic Nanostructured Cellulose and Cellulose Composites. *Handbook of Nanocellulose and Cellulose Nanocomposites* 2 (2017): 731-760.
  - [127] M. Kaushik, A. Moores, Review: Nanocelluloses as versatile supports for metal nanoparticles and their applications in catalysis, *Green Chem.* 18 (2016) 622–637.
  - [128] S.N. Das, J.H. Choi, J.P. Kar, J.M. Myoung, Tunable and reversible surface wettability transition of vertically aligned ZnO nanorod arrays, *Appl. Surf. Sci.* 255 (2009) 7319–7322.

## Chapter 2

# Preparation of ZnO/TOCN nanocomposite films and property investigation of the films with different ZnO contents

### 2.1 Abstract

ZnO particle/water and 2,2,6,6-tetramethylpiperidine-1-oxyl (TEMPO)-oxidized cellulose nanofibril (TOCN)/water dispersions were mixed at various ratios under stirring. The aqueous ZnO/TOCN mixtures were sonicated, cast, and dried to prepare ZnO/TOCN composite films with various ZnO/TOCN weight ratios. The ZnO contents of the films were controlled to 0–50% (w/w). When the ZnO content was increased to 5–50%, the porosity of the composite films increased to 14–23%. This is probably because the positively charged ZnO particles and negatively charged TOCN elements formed aggregates in both aqueous mixtures and dried films. The ZnO/TOCN composite film of thickness 10  $\mu\text{m}$  containing 10% ZnO had more than 80% light transmittance at 600 nm, and high UV-screening properties. The composite films containing 25 and 50% ZnO had almost perfect UV-screening properties, but their light transmittances at 600 nm were only 60–80%. All the composite films had low coefficients of thermal expansion ( $<10$  ppm/K). Because the composite films consisted of stiff TOCNs and ZnO, but had porous structures, the tensile strength and strain-to-failure decreased slightly with increasing ZnO content from 0 to 10%. The composite film containing 50% ZnO had explicitly ductile properties because of its high porosity.

### 2.2 Introduction

Organic/inorganic nanocomposites have been extensively studied to effectively impart the properties of inorganic materials, such as thermal stability, flame retardancy, mechanical properties, and gas barrier properties to polymer matrices [1–3]. ZnO is one of the most widely used inorganic additives to polymer matrices in the preparation of organic/inorganic nanocomposites because ZnO nanomaterials have unique physical and chemical properties such as fluorescence emission [4],

piezoelectricity [5], UV absorption and scattering [6–8], photocatalytic activity [9], and antimicrobial activity [10]. ZnO nanomaterials, especially ZnO nanoparticles, are therefore widely used in synthetic rubbers, paint, batteries, and flame retardants.

Cellulose is the most abundant biopolymer and is expected to partly replace fossil-based synthetic polymers. This will reduce environmental burdens and the consumption of non-renewable resources. In recent years, various chemical, enzymatic, and other pretreatments of wood cellulose fibers for efficiently preparing various nanocelluloses [cellulose nanocrystals (CNCs) and cellulose nanofibrils] have been reviewed [11–15]. In these review papers, it has been reported that nanocelluloses, which are bio-based nanomaterials, have unique characteristics, which differ from those of conventional fossil-based or inorganic nanomaterials. ZnO/nanocellulose composites have been prepared to impart these ZnO functions to nanocelluloses, primarily using the following procedures: in situ ZnO nanoparticle formation through hydrolysis of zinc alkoxides in the presence of nanocellulose, and mechanical mixing of ZnO nanoparticles in aqueous nanocellulose dispersions [16–20]. The in situ preparation of ZnO/nanocellulose composites was reported to give a broad size distribution of ZnO particles [16]. In contrast, commercial ZnO nanoparticles have narrow size distributions. Mixing commercially available ZnO nanoparticles with aqueous nanocellulose dispersions is therefore promising, if ZnO particles can be homogeneously distributed in the nanocellulose matrix. Lizundia et al. [19] reported that ZnO/CNC composite films are more hydrophobic and have higher thermal stabilities and elastic moduli compared with neat CNC films. However, because CNCs have spindle-like morphologies with low aspect ratios, flexible ZnO/CNC composite films with good mechanical properties cannot be obtained. 2,2,6,6-Tetramethylpiperidine-1-oxyl (TEMPO) is a water-soluble, stable nitroxyl radical, and TEMPO-mediated oxidation of native celluloses under appropriate conditions enables oxidized celluloses to be converted to TEMPO-oxidized cellulose nanofibrils (TOCNs) of homogeneous width ~3 nm by gentle mechanical disintegration in water [21,22]. Because TOCNs prepared from softwood bleached kraft pulp (SBKP) have high aspect ratios (>150) and are completely dispersed in water at the individual nanofibril level, TOCN films prepared from TOCN/water dispersions by casting and drying have high transparencies (>80% at 600 nm), good mechanical properties (elastic moduli of 6–7 GPa and tensile strengths of 200–300 MPa), low coefficients of thermal expansion (~3 ppm/K), and low oxygen transmission rates under dry conditions [ $\sim 0.001 \text{ mL } \mu\text{m}/(\text{m}^2 \text{ days kPa})$ ] [13,23]. ZnO/TOCN composite films are therefore expected to have



better optical and mechanical properties than other ZnO/nanocellulose composite films, together with the functions of ZnO nanoparticles.

In this study, ZnO/TOCN composite films were prepared by mixing commercial ZnO nanoparticle/ water and TOCN/water dispersions at various ratios. ZnO/TOCN composite films were prepared from the aqueous mixtures by casting and drying. The fundamental properties, namely the optical, thermal, hydrophilic/hydrophobic, and mechanical properties, of ZnO/TOCN films with ZnO contents of 0–50% (w/w) were investigated.

## **2.3 Materials and methods**

### **2.3.1 Materials**

A never-dried SBKP supplied by Nippon Paper (Tokyo, Japan) was demineralized with hydrochloric acid in water at pH 2 for 2 h before use [24]. TEMPO and ZnO particle dispersions [50% (w/w) in water] were purchased from Sigma-Aldrich (USA). NaBr, 2 M NaClO solution, NaOH, NaBH<sub>4</sub> were laboratory grade (Wako Pure Chemical Ind., Osaka, Japan) and used without further purification.

### **2.3.2 Preparation of TOCN dispersion**

Fibrous TEMPO-oxidized cellulose (TOC) was prepared from SBKP using a TEMPO/NaBr/NaClO system containing NaClO at 5 mmol/g-SBKP in water at pH 10 [24] and room temperature for 3 h. Post reduction of the same mixture was performed (as a one-pot reaction) with NaBH<sub>4</sub> (0.1 g/ g-SBKP) to reduce the small amounts of C6-aldehydes and C2/C3 ketones present in the TOC to alcohols by stirring the mixture at pH 10 for 3 h (Takaichi et al. 2014). The obtained TOC was washed repeatedly with water by filtration. A TOC/water slurry was mechanically disintegrated to prepare a completely individualized 0.1% (w/v) TOCN/water dispersion. Unfibrillated fractions were removed by centrifugation at 12,000g for 15 min. The TOCN concentration in the dispersion was adjusted to 0.1% (w/v) using a rotary evaporator at 40 °C [25].

### **2.3.3 ZnO/TOCN composite films**

The 50% (w/w) aqueous ZnO particle dispersion was diluted to 2% (w/v) with water and

sonicated for 1 h using an ultrasonic bath (M1800-J; Yamato Scientific, Tokyo, Japan). The ZnO/water dispersion was added to the 0.1% (w/v) TOCN/water dispersion (30 mL) under vigorous agitation using a magnetic stirrer. After 30 min, the mixture was homogenized in the ultrasonic bath for 1 h. These stirring and sonic treatments were repeated once. The obtained ZnO/ TOCN/water dispersion was poured into a Petri dish of diameter 50 mm and dried in an oven at 40 °C for 3 days. The cast and dried films were carefully peeled off from the Petri dish and stored in a conditioning room at 23 °C and 50% relative humidity (RH). The composite films with ZnO:TOCN weight ratios of 1:99, 5:95, 10:90, 25:75, and 50:50 are denoted by ZT-1, ZT-5, ZT-10, ZT-25, and ZT-50, respectively.

### 2.3.4 Characterization

The average particle sizes and  $\zeta$ -potentials of the ZnO nanoparticles were determined using a particle analyzer (Delsa Nano HC, Beckman Coulter, Germany). Scanning electron microscopy (SEM) was used to examine the composite film surfaces and cross sections using a Hitachi S4800 field-emission microscope at 1.0 kV, after osmium coating using a Meiwafoysis Neoc-ST osmium coater at 5 mA for 10 s. Cross sections of the composite films were examined by transmission electron microscopy (TEM) using a JEOL JEM-2000EX microscope at 200 kV. The films were embedded in a resin and sectioned perpendicularly to the film surface using a Leica Ultracut E microtome equipped with a glass knife. Sections of thickness approximately 100 nm were cut for observations. X-ray diffraction (XRD) patterns of the composite films were obtained using a Rigaku RINT 2000 diffractometer with monochromator-filtered Cu K $\alpha$  radiation ( $\lambda = 1.5418 \text{ \AA}$ ) at 40 mV and 40 mA. Ultraviolet–visible (UV–vis) light transmittance spectra of the composite films were recorded using a V-670 spectrophotometer (JASCO, Japan). The coefficients of thermal expansion (CTE) of the composite films were measured using a thermomechanical analyzer (TMA-60, Shimadzu, Japan) at a 0.03 N loading in a nitrogen flow at 50 mL/min from 30 to 150 °C at 5 °C/min. Thermogravimetric (TG) curves of the composite films were obtained at 50–500 °C at 5 mL/min using a TG apparatus (Thermoplus TG8120, Rigaku, Japan) with a nitrogen flow. Every sample was tested at a heating rate of 5 °C/min. The contact angle of a 2  $\mu$ L water droplet on the film surface that was in contact with the Petri dish surface during cast-drying was measured at 23 °C and 50% RH using a Kyowa FAMAS DM500 apparatus (Saitama, Japan); five measurements were performed for each sample. The surface roughness (root-meansquare roughness,  $R_q$ ) of the films were determined from atomic force

microscopy (AFM) height profiles obtained under ambient conditions using a Veeco NanoScope III instrument (Digital Instruments, New York, USA) operated in tapping mode. The film lower surface was used for the  $R_q$  measurements. Tensile tests were performed using a tester (EZ-TEST, Shimadzu, Japan) equipped with a 500 N load cell at 23 °C and 50% RH. Rectangular specimens ( $20 \times 2 \text{ mm}^2$ ) were cut from the composite films, and were subjected to tensile tests with a 10 mm span length at a 1.0 mm/min speed. At least six measurements were performed for each sample.

## **2.4 Results and discussion**

### **2.4.1 Fundamental properties**

The average particle size and  $\zeta$ -potential of the ZnO particles in water were 65.8 nm with a polydispersity index of 0.219, and +28.5 mV, respectively. Because each TOCN element has negatively charged sodium carboxylate groups densely and regularly present on the surface, its  $\zeta$ -potential in water is -80 mV [13,26]. Cationic ZnO particles can therefore be homogeneously adsorbed on the anionic TOCN surfaces. However, it is also possible for positively charged ZnO particles to form aggregates with anionic TOCN elements by the formation of ionic linkages between these two components in water. Homogenous mixing is therefore required for preparing ZnO/TOCN composite films. Because agitation of the aqueous TOCN dispersions using a magnetic stirrer bar was not sufficient to completely disperse the ZnO particles in the mixtures, the ZnO/TOCN mixtures were subjected to mild sonication with an ultrasonic bath after stirring. No ZnO flocs were visible in the mixtures after sonication. ZnO/TOCN composite films were then prepared by casting and drying.

**Table 2.1.** Theoretical and measured densities and moisture contents of ZnO/TOCN composite films conditioned at 23 °C and 50% RH.

	ZnO/TOCN weight ratio	Theoretical film density (g/cm <sup>3</sup> ) <sup>a</sup>	Measured film density (g/cm <sup>3</sup> ) <sup>b</sup>	Moisture content (wt%)	Film porosity (vol%) <sup>c</sup>
ZT-0	0/100	1.60	1.56	3.77	2.5
ZT-1	1/99	1.61	1.51	6.48	6.3
ZT-5	5/95	1.66	1.42	9.32	14.4
ZT-10	10/90	1.72	1.42	9.13	17.6
ZT-25	25/75	1.95	1.49	8.14	23.5
ZT-50	50/50	2.49	1.95	6.16	21.7

<sup>a</sup> Calculated from densities of pure ZnO and TOCN, and ZnO/TOCN weight ratio without considering pore volume.

<sup>b</sup> Measured from weight and volume of composite films.

<sup>c</sup> Calculated from the measured densities of composite films.

Table 2.1 shows the calculated and measured densities, water contents, and porosities of the ZnO/TOCN composite films. The ZT-0, i.e., the neat TOCN film, had a density of 1.56 g/cm<sup>3</sup>, which closes to the corresponding theoretical value (1.6 g/cm<sup>3</sup>) for cellulose I crystallites [27]. Each measured film density was lower than the corresponding calculated value, as the ZnO content increased. This shows that the pore volume in the film increased with increasing ZnO content. No such increases in porosity with increasing the nanoclay content were observed for nanoclay/TOCN composite films [28,29]; therefore some ZnO particles may have aggregated in the composite films. Details to calculate porosities of the ZnO/TOCN composite films from their densities are described in the Appendix with Eqs. (2A.1-6) and Table 2A.1.

SEM images of the ZT-5, ZT-10, ZT-25, and ZT-50 film surfaces, and TEM images of cross sections of the ZT-25 film are shown in Figure 2.1 and 2.2, respectively. The average ZnO particle size was 65.8 nm, determined using a particle analyzer. Although the ZT-5 film consisted of ZnO particles mostly dispersed at the individual particle level on the composite surface, clear aggregation of ZnO

particles was observed on the other composite film surfaces. The high porosities of the composite films with high ZnO contents ([Table 2.1](#)) are therefore probably caused by not only the pore structures inside the films but also their high surface roughness. The TEM images of the ZT-25 film show that some ZnO particles were aggregated in the film. These results support the porosity data shown in [Table 2.1](#); aggregation of ZnO particles in the composite films increased with increasing ZnO content. The positively charged ZnO particles can aggregate with the anionic TOCN elements in water. The porous structures of the ZnO/TOCN composite films were further investigated by SEM observations of film cross sections ([Figure 2A.1](#) in the Appendix). The ZT-0 film had a dense structure with no pores in the cross section, whereas the ZT-25 film had a clear porous structure. Aggregation behavior between cationic ZnO particles and anionic TOCN elements may therefore have caused the porous structures shown in [Table 2.1](#) and [Figure 2A.1](#).

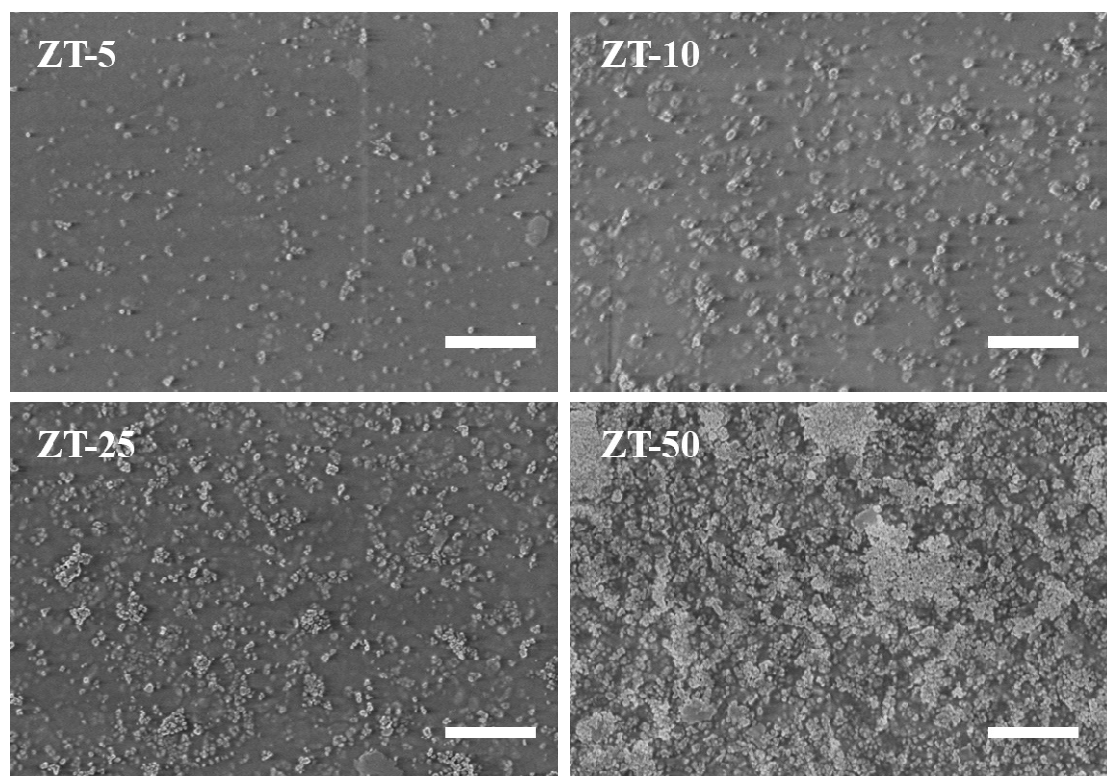


**Figure 2.1.** SEM images of ZnO/TOCN composite film surfaces. (Scale bar = 1 μm)

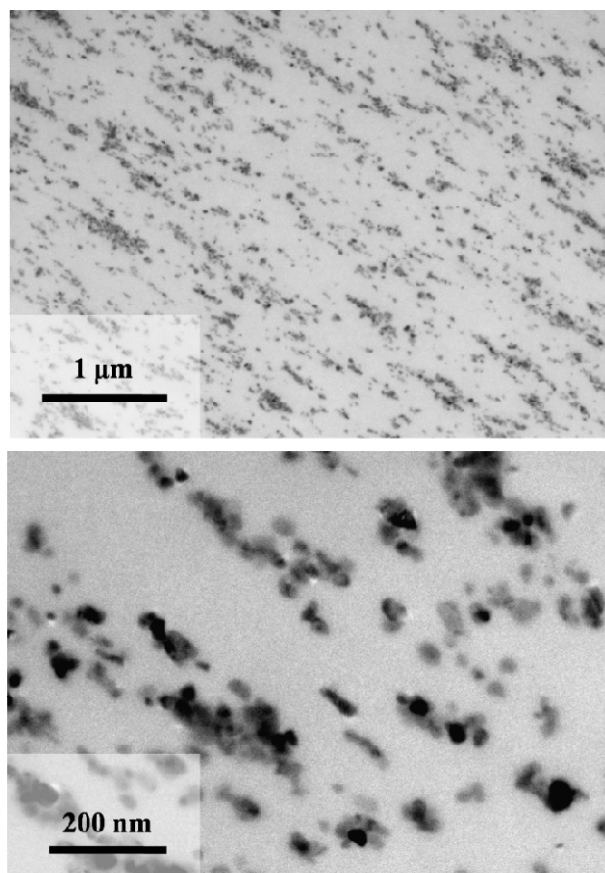


**Figure 2.2.** TEM images of cross sections of ZnO/TOCN (25:75 by weight) composite film

XRD patterns of the ZnO/TOCN composite films are shown in [Figure 2A.2](#) in the Appendix. Typical diffraction peaks for wurtzite-type ZnO crystallites were observed at  $2\theta$  greater than  $30^\circ$  together with peaks from cellulose I in the TOCNs [30]. The intensities of the ZnO peaks increased with increasing ZnO content, and those of cellulose I decreased.

## 2.4.2 Optical properties of ZnO/TOCN composite films

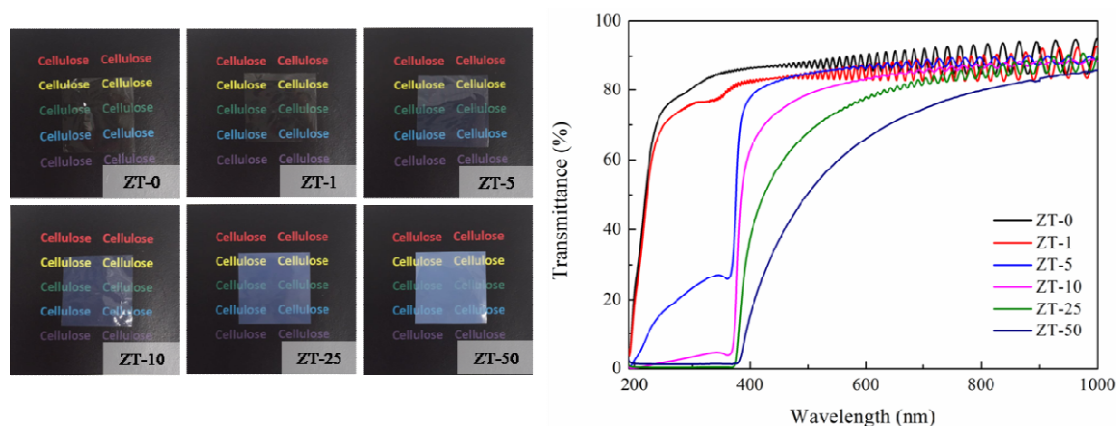


**Figure 2.3.** Appearance and UV-vis light transmittance spectra of ZnO/TOCN composite films with normalized thickness of 10  $\mu\text{m}$

Figure 2.3 shows UV–vis light transmittance spectra of the composite films normalized to a 10  $\mu\text{m}$  thickness. The ZT-1, ZT-5, and ZT-10 films had high visible light transmittances or transparencies of more than 80% at 600 nm. The ZT-25 and ZT-50 films had 60–80% transmittances at 600 nm. The ZT-10, ZT-25, and ZT- 50 films also clearly showed UV-light-screening properties, and the ZT-5 composite film showed high UV-light-screening properties. The ZT-10, ZT-25, and ZT-50 could therefore be used for screening UVA light at 320–400 nm, UV-B light at 280–320 nm, and UV-C light at 100–280 nm. Because UV-A and UV-B light seriously damage biological cells and DNA via absorption by cellular DNA, secondary photoreactions of existing DNA photoproducts, or damage of DNA by indirect photosensitizing reactions [31], the ZnO/TOCN composite films may have applications in films that are transparent to visible light but protect against UV light for biological safety.

### 2.4.3 Thermal properties of ZnO/TOCN composite films

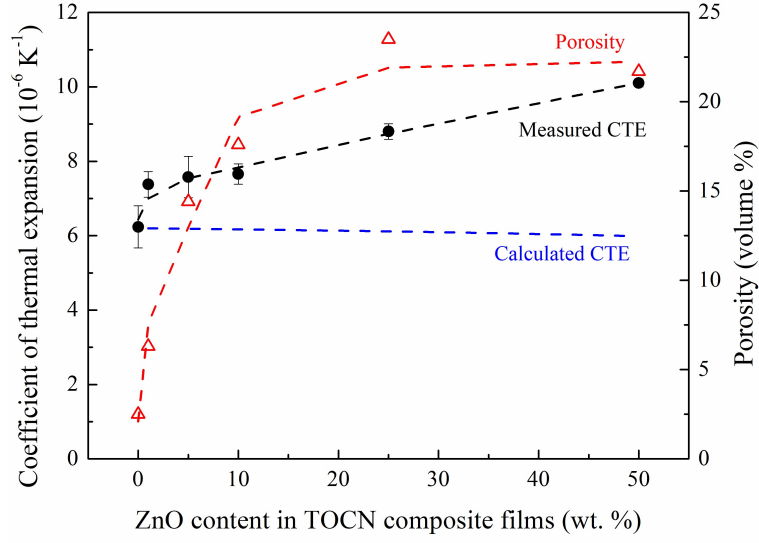


**Figure 2.4.** CTEs and porosities of ZnO/TOCN composite films

Thermal properties of the ZnO/TOCN composite films were investigated in terms of dimensional stability and mass stability, using CTE and TG analyses, respectively. Figure 2.4 shows the measured and calculated CTE values for the ZnO/TOCN composite films, together with the film porosities shown in Table 2.1. The CTE value increased with increasing ZnO content. The wurtzite-type ZnO and TOCN have CTE values of  $5.23 \times 10^{-6}/\text{K}$  [32] and  $6.24 \times 10^{-6}/\text{K}$  (obtained in this study for the ZT-0 film), respectively. The CTE values for the composite films can be estimated from the CTE values and volume ratios of the two components using the following Eq. (2.1) [33],

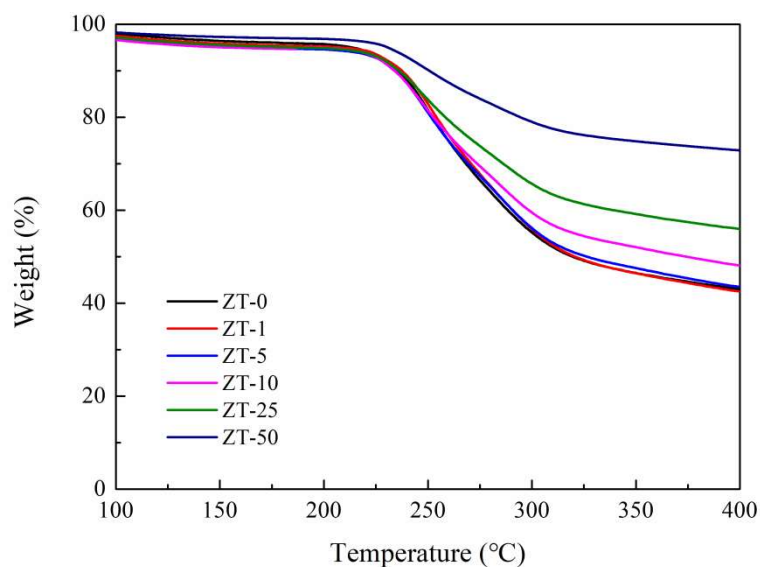
$$\alpha_c = \alpha_f V_f + \alpha_m (1 - V_f) \quad (2.1)$$

where  $\alpha_c$ ,  $\alpha_m$  and  $\alpha_f$  are the CTEs of the composite film, TOCN, and ZnO, respectively, and  $V_f$  is the volume fraction of ZnO in the composite film. Here, Grüneisen parameters parallel and perpendicular to the longitudinal ZnO crystallite were assumed to be the same, because these two values are quite similar [34]. The volume fraction ratios of ZnO and TOCNs in the composite films were calculated using TOCN and ZnO densities of  $1.6$  [27] and  $5.6 \text{ g/cm}^3$  [35], respectively.

The calculated CTE values in Figure 2.4 were lower than the corresponding measured CTE values for each ZnO content. This discrepancy between the experimental and calculated CTE values depending on the ZnO content of the composite film is probably caused by high porosities or air fraction volumes of the composite films. The air volume in the films should increase with temperature



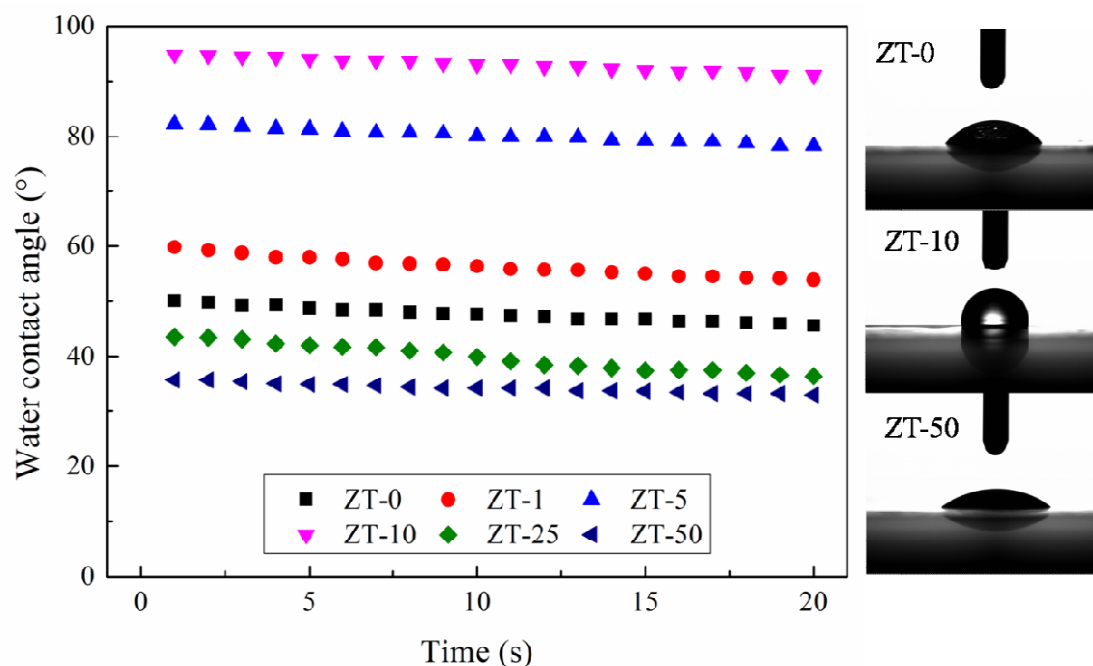
at a constant pressure, according to Charles's law [36]. The porosities of the composite films shown in Figure 2.4 are roughly correlated to the measured CTE values. However, the CTE values of the composite films were sufficiently low ( $\leq 10$  ppm/K), and had high thermal dimensional stability up to 150 °C.



**Figure 2.5.** TG curves of ZnO/TOCN composite films, obtained at 5 °C/min

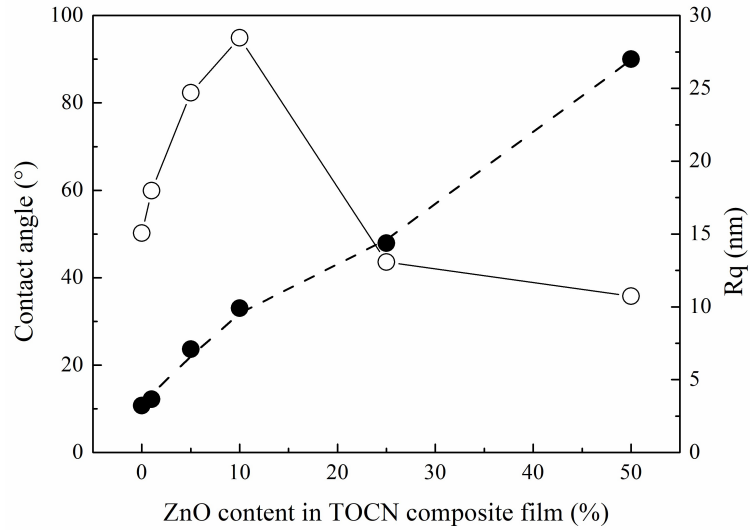
Figure 2.5 shows TG curves of the ZnO/TOCN composite films, obtained at 5 °C/min. All the composite films had thermal degradation onset temperatures of ~230 °C, irrespective of the ZnO content. The presence of ZnO therefore had almost no effect on the thermal degradation point of the TOCNs. Because ZnO is thermally stable up to 400 °C, the differences among the weight decrease ratios at temperatures >250 °C of the composite films can be explained in terms of the different ZnO contents; the higher the ZnO content, the lower the weight decrease ratio at temperatures >250 °C.

#### 2.4.4 Surface hydrophilic and hydrophobic properties of ZnO/TOCN composite films



**Figure 2.6.** WCAs on ZnO/TOCN composite film surfaces

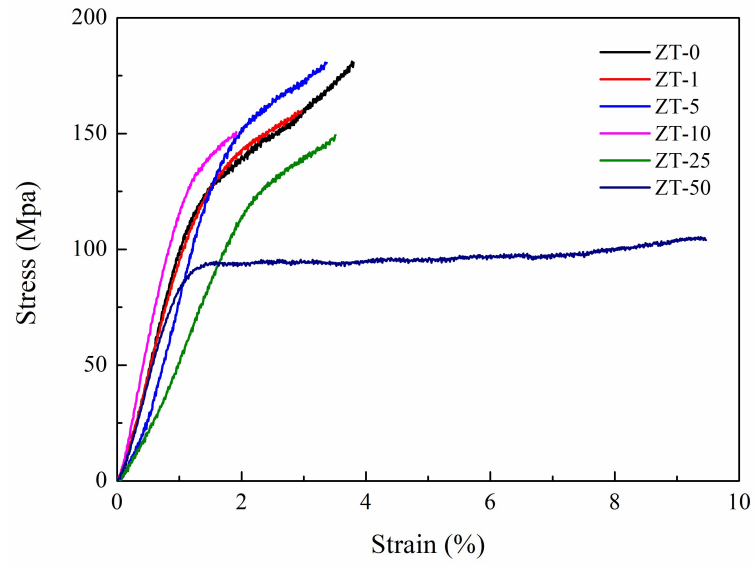
Figure 2.6 shows the water contact angles (WCAs) on the ZnO/TOCN composite film surfaces. The WCA value increased from 50° to 95° i.e., the film hydrophobicity improved with increasing ZnO content from 0% to 10% then decreased to below 50° i.e., the film became hydrophilic again, at ZnO contents of 25% and 50%. Because the TOCNs and ZnO are both hydrophilic, it is unusual for the hydrophilic ZnO/TOCN composite film surfaces to become hydrophobic. This anomaly can be explained in terms of the surface roughness of the composite film or the presence of small air fractions on the film surface, according to Cassie's law [36,37], as was observed for nanoclay/TOCN composite films [38].



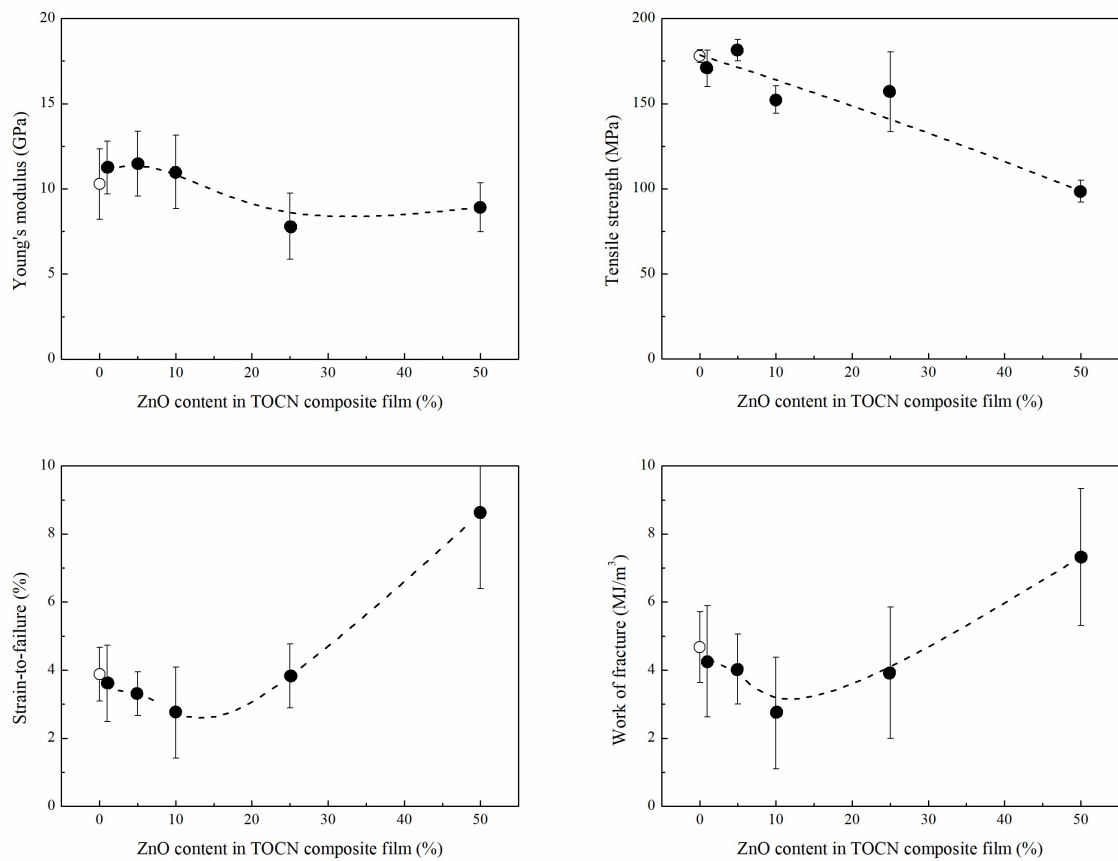
**Figure 2.7.** Relationships between ZnO content of composite films and either WCA in Figure 2.6 or root-mean-square roughness ( $R_q$ ) determined using AFM

Figure 2.7 shows the relationship between the ZnO content and either the WCA (shown in Fig. 2.6) or  $R_q$  value (determined using AFM) of the composite film surface. The  $R_q$  increased almost linearly with increasing ZnO content, but the WCA was maximum at a ZnO content of 10%. The balance between the areas of the hydrophilic ZnO/TOCN fraction and hydrophobic air fraction (with WCA  $\approx 180^\circ$ ) on the surface may have resulted in the hydrophilic/hydrophobic nature of the composite films shown in Figs. 2.6 and 2.7. Details are described in the Appendix with Eqs. (2A.7 and 2A.8) and Figure 2A.3 [38].

## 2.4.5 Mechanical properties



**Figure 2.8.** Typical stress–strain curves of ZnO/TOCN composite films



**Figure 2.9.** Tensile properties of ZnO/TOCN composite films

The typical strain–stress curves and the corresponding tensile properties are shown in [Figures 2.8](#) and [2.9](#), respectively. Because the composite films with higher ZnO contents had higher porosities ([Table 2.1](#); [Figure 2.4](#)), the films consisted of three components, i.e., ZnO, TOCNs, and pores. Interpretation of the tensile properties of the composite films is therefore not simple. The high ductile properties of the ZT-50 film may have been caused by its high porosity, resulting from its high ZnO content (50%). The air voids in the host matrix (TOCN in this case) assist in releasing the volume strain and reduce the sensitivity towards crack formation [\[39,40\]](#). For the composite films with 1–10% ZnO contents, the Young’s moduli were higher, and the tensile strengths and strain-to-failure values were slightly lower than those of the ZT-0 film; this differs from the trend observed for nanoclay/TOCN composite films [\[28,38\]](#). The aggregation behavior of the positively charged ZnO particles in the TOCN matrix may have resulted in the tensile properties shown in [Figures 2.8](#) and [2.9](#). In the case of nanoclay/TOCN composite films with 5–10% nanoclay contents, the tensile strengths and strain-to-failure values were more than twice those of the neat TOCN film. These differences between the mechanical properties of ZnO/TOCN and nanoclay/TOCN films probably arise because the differences between the particle morphologies and/or surface charges of nanoclay and ZnO result in differences between the pore structures of the two composite systems.

#### 2.4.6 Antimicrobial activity

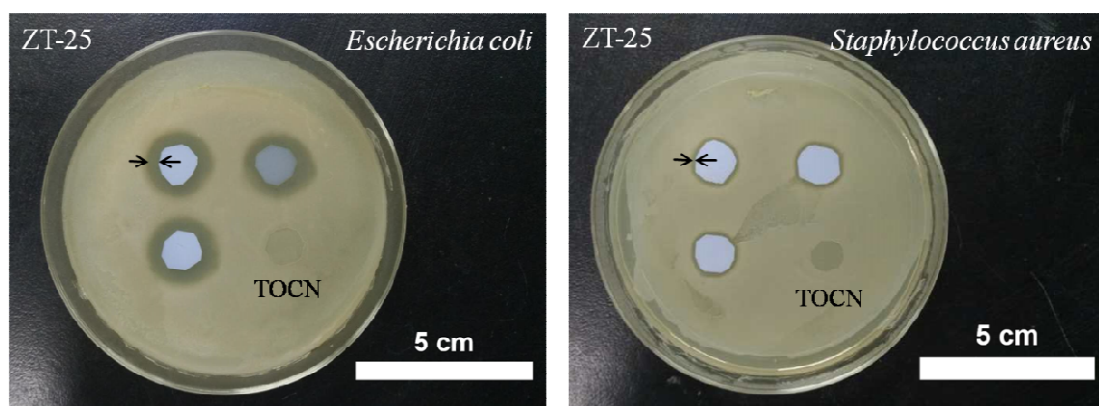


**Figure 2.10.** Inhibition zones of ZnO/TOCN (25:75 by weight) composite films and neat TOCN films towards *Escherichia coli* and *Staphylococcus aureus*.

The antimicrobial activity of ZnO/TOCN composite films towards gram-negative bacterium *Escherichia coli* and gram-positive bacterium *Staphylococcus aureus* were tested by the inhibition zone

method. As shown in [Figure 2.10](#), obvious inhibition zones were observed around the ZnO/TOCN composite films, which indicated that the ZnO/TOCN composite films have effective antibacterial activity, whereas neat TOCN films did not exhibit antimicrobial activity. Since the inhibition zone diameter of *Escherichia coli* is larger than *Staphylococcus aureus*, the antibacterial performance of ZnO/TOCN composite films are especially effective towards gram-negative bacterium.

## 2.5 Conclusions

ZnO/TOCN composite films with 0–50% ZnO contents were prepared by mixing ZnO/water and TOCN/ water dispersions at various weight ratios, stirring, sonicating, and subsequent casting and drying. The porosity of the composite films increased from 2.5 to 14–24% with increasing ZnO content to above 5%. The aggregation of cationic ZnO particles and anionic TOCN elements may have caused the porous structures of the composite films. The ZT-10 film of thickness 10  $\mu\text{m}$  had a high transparency (more than 80% at 600 nm) and high UV-screening properties. The ZT-25 and ZT-50 films had almost perfect UV screening properties, but the light transmittances at 600 nm were 60–80%. The composite films had low CTEs ( $<10$  ppm/K), although the CTE value increased with increasing ZnO content, probably because of the high film porosities. Because the composite films consisted of stiff TOCNs and ZnO, and soft air components, the tensile strength and strain-to-failure decreased slightly with increasing ZnO content from 0 to 10%. The ZT-50 film had explicitly ductile properties because of its high porosity.

## 2.6 Appendix

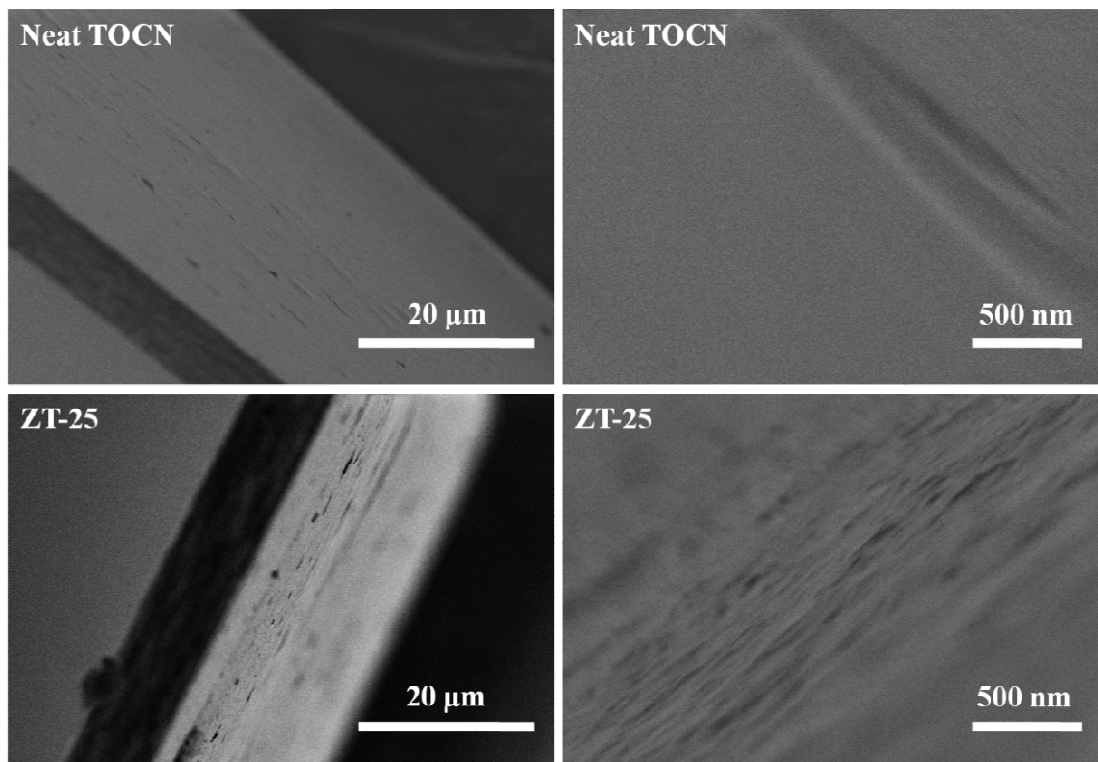


**Figure 2A.1.** SEM images of cross sections of neat TOCN and 25%-ZnO-containing TOCN films

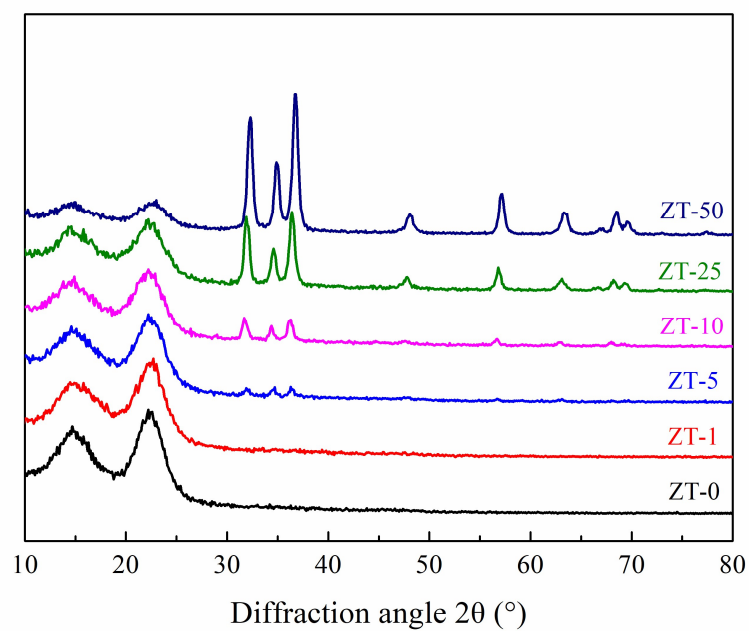


**Figure 2A.2.** XRD patterns of ZnO/TOCN composite films

## Calculation of porosities of ZnO/TOCN composite films

Each ZnO/TOCN composite film consists of ZnO nanoparticles, TOCNs, and pores. The composite film density  $\rho_c$  can be expressed as the following Eq. (2A.1),

$$\rho_c = \frac{m_c}{V_c} = \frac{m_{ZnO} + m_{TOCN} + m_{pore}}{V_{ZnO} + V_{TOCN} + V_{pore}} \quad (2A.1)$$

Where  $m_c$  and  $V_c$  are the weight and volume, respectively, of a composite film. The values of  $m_{ZnO}$  and  $m_{TOCN}$  and  $m_{pore}$  are the weights of ZnO, TOCN, and pore (or air), respectively, in the composite film;  $V_{ZnO}$ ,  $V_{TOCN}$ , and  $V_{pore}$  are the volumes of ZnO, TOCN, and pore, respectively, in the composite film. The  $V_{pore}$  should be taken into account for calculation of the  $\rho_c$  value, whereas  $m_{pore}$  has no weight. The Eq. (2A.1) can be therefore expressed as the following Eq. (2A.2).

$$\rho_c = \frac{m_c}{V_c} = \frac{m_{ZnO} + m_{TOCN}}{V_{ZnO} + V_{TOCN} + V_{pore}} \quad (2A.2)$$

Moreover,  $V_{ZnO}$  and  $V_{TOCN}$  can be expressed as the following Eqs. (2A.3) and (2A.4).

$$V_{ZnO} = \frac{m_{ZnO}}{\rho_{ZnO}} \quad (2A.3)$$

$$V_{TOCN} = \frac{m_{TOCN}}{\rho_{TOCN}} \quad (2A.4)$$

Hence, the  $V_{pore}$  can be expressed as the following Eq. (2A.5) from Eq. (2A.2) using Eqs. (2A.3) and (2A.4).

$$V_{pore} = \frac{m_{ZnO} + m_{TOCN}}{\rho_c} - \frac{m_{ZnO}}{\rho_{ZnO}} - \frac{m_{TOCN}}{\rho_{TOCN}} \quad (2A.5)$$

The  $\rho_{ZnO}$  and  $\rho_{TOCN}$  values of 5.606 and 1.6 g/cm<sup>3</sup>, respectively, have been reported in the literature and used in this study. The  $m_{TOCN}$  is a constant value of 0.03 g for all the composite films prepared in this study. The  $m_{ZnO}$  values varied for the ZnO/TOCN composite films prepared with various ZnO contents.

The porosities of the composite films can therefore be calculated from the following Eq. (2A.6):

$$\text{Porosity (vol. \%)} = \frac{V_{pore}}{V_c} \times 100\% = \frac{V_{pore}}{V_{ZnO} + V_{TOCN} + V_{pore}} \times 100\% \quad (2A.6)$$



**Table 2A.1.** The parameters for calculation of porosities of ZnO/TOCN composite films

	ZnO/TOCN	$m_{\text{TOCN}}$	$m_{\text{ZnO}}$	$\rho_c$	$V_{\text{pore}}$	Porosity
	weight ratio	(g)	(g)	(g/cm <sup>3</sup> ) <sup>a</sup>	(cm <sup>3</sup> )	(vol.%)
ZT-0	0/100	0.03	0	1.56	$0.48 \times 10^{-3}$	2.5
ZT-1	1/99		$0.3 \times 10^{-3}$	1.51	$1.26 \times 10^{-3}$	6.3
ZT-5	5/95		$1.57 \times 10^{-3}$	1.42	$3.21 \times 10^{-3}$	14.4
ZT-10	10/90		$3.33 \times 10^{-3}$	1.42	$4.13 \times 10^{-3}$	17.6
ZT-25	25/75		$10.0 \times 10^{-3}$	1.49	$6.31 \times 10^{-3}$	23.5
ZT-50	50/50		$30.0 \times 10^{-3}$	1.95	$6.67 \times 10^{-3}$	21.7

<sup>a</sup> Measured from the weight and volume of each composite film

### Relationship between the water contact angle and roughness of ZnO/TOCN composite film surfaces

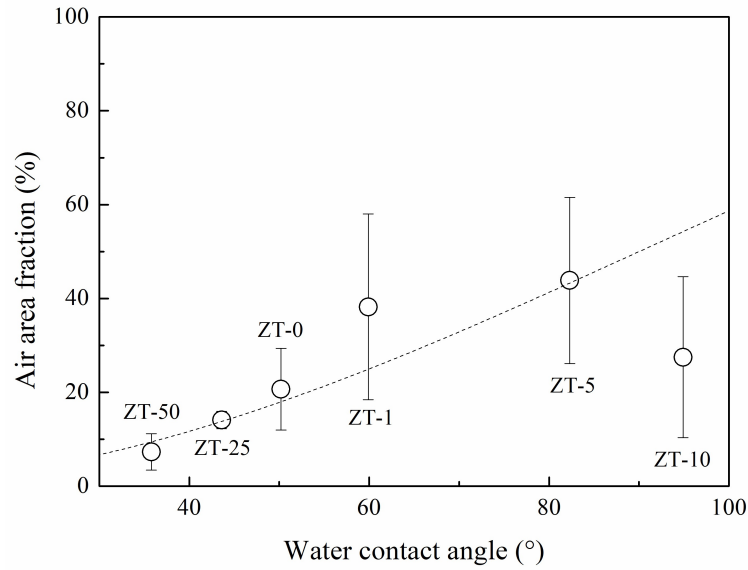


**Figure 2A.3.** The relationship between the WCA and air area fraction of ZnO/TOCN composite film surfaces obtained at  $0.3R_{\text{max}}$  bearing height. The dashed line indicates the theoretical value calculated using Eq. (2A.8) and  $0.3R_{\text{max}}$ .

In the case of non-flat ZnO/TOCN composite film surfaces as shown in Figure 2.1, the water contact angle (WCA) of the composite film surface  $\theta_c$  can be expressed according the following Cassie's law, Eq. (2A.7),

$$\cos \theta_c = f_1 \cos \theta_1 + f_2 \cos \theta_2 \quad (2A.7)$$

where  $\theta_1$  and  $\theta_2$  are the WCAs on ideally flat surfaces of the fractions 1 and 2, respectively, which constitute the film surfaces at area fraction ratio of  $f_1 : f_2$ , respectively ( $f_1 + f_2 = 1$ ). The ZnO and TOCN fraction contributes to the hydrophilic surface, and the air fraction does to the hydrophobic surface. Thus, in the case of the ZnO/TOCN composite films, the values  $\theta_1$  and  $\theta_2$ , which originate from ZnO/TOCN and air fractions, can be regarded as  $0^\circ$  and  $180^\circ$ , respectively. Then, Eq. (2A.7) can be expressed as the following Eq. (2A.8).

$$\cos \theta_c = 1 - 2\theta_{\text{air}} \quad (2A.8)$$

The air area fraction on the film surface was geographically calculated using the bearing analysis function with an atomic force microscopy (AFM) software, from the root-mean-square roughness ( $R_q$ ) and power spectral density of the film surface calculated from the AFM height profile [38,41,42]. The relationship between the WCAs of the ZnO/TOCN composite film surfaces and their air fractions is plotted in the Figure 2A.3, assuming that the bearing height of the composite film is  $0.3R_{\text{max}}$ . The  $R_{\text{max}}$  value is the difference between the highest and the lowest positions of the nanostructured surface obtained by the bearing analysis. The dashed line in Figure 2A.3 shows the relationship calculated using Eq. (2A.8) and the  $0.3R_{\text{max}}$  value, which had the best correlation between WCAs and air area fractions for the ZnO/TOCN composite films among the other  $R_{\text{max}}$  values such as  $0.2R_{\text{max}}$ ,  $0.4R_{\text{max}}$  and  $0.6R_{\text{max}}$  [38].

## 2.7 References

- [1] X. Ma, P.R. Chang, J. Yang, J. Yu, Preparation and properties of glycerol plasticized-pea starch/zinc oxide-starch bionanocomposites, *Carbohydr. Polym.* 75 (2009) 472–478.
- [2] W. Tang, M.H. Santare, S.G. Advani, Melt processing and mechanical property characterization of multi-walled carbon nanotube/high density polyethylene (MWNT/HDPE) composite films, *Carbon*. 41 (2003) 2779–2785.
- [3] J.W. Gilman, Flammability and thermal stability studies of polymer layered-silicate (clay) nanocomposites, *Appl. Clay Sci.* 15 (1999) 31–49.
- [4] H.M. Xiong, Y. Xu, Q.G. Ren, Y.Y. Xia, Stable aqueous ZnO@polymer core-shell nanoparticles with tunable photoluminescence and their application in cell imaging, *J. Am. Chem. Soc.* 130 (2008) 7522–7523.
- [5] Q. Yang, Y. Liu, C. Pan, J. Chen, X. Wen, Z.L. Wang, Largely enhanced efficiency in ZnO nanowire/p-polymer hybridized inorganic/organic ultraviolet light-emitting diode by piezo-phototronic effect, *Nano Lett.* 13 (2013) 607–613.
- [6] M.M.A. El-Hady, A. Farouk, S. Sharaf, Flame retardancy and UV protection of cotton based fabrics using nano ZnO and polycarboxylic acids, *Carbohydr. Polym.* 92 (2013) 400–406.
- [7] O.M. El-Feky, E.A. Hassan, S.M. Fadel, M.L. Hassan, Use of ZnO nanoparticles for protecting oil paintings on paper support against dirt, fungal attack, and UV aging, *J. Cult. Herit.* 15 (2014) 165–172.
- [8] Y.Q. Li, S.Y. Fu, Y.W. Mai, Preparation and characterization of transparent ZnO/epoxy nanocomposites with high-UV shielding efficiency, *Polymer*. 47 (2006) 2127–2132.
- [9] D. Chen, Z. Wang, T. Ren, H. Ding, W. Yao, R. Zong, Y. Zhu, Influence of defects on the photocatalytic activity of ZnO, *J. Phys. Chem. C*. 118 (2014) 15300–15307.
- [10] S. Shankar, J.P. Reddy, J.W. Rhim, H.Y. Kim, Preparation, characterization, and antimicrobial activity of chitin nanofibrils reinforced carrageenan nanocomposite films, *Carbohydr. Polym.* 117 (2015) 468–475. doi:10.1016/j.carbpol.2014.10.010.
- [11] D. Klemm, F. Kramer, S. Moritz, T. Lindström, M. Ankerfors, D. Gray, A. Dorris, Nanocelluloses: a new family of nature-based materials, *Angew. Chemie*. 50 (2011) 5438–5466.
- [12] R.J. Moon, A. Martini, J. Nairn, J. Simonsen, J. Youngblood, Cellulose nanomaterials review: structure, properties and nanocomposites, *Chem. Soc. Rev.* 40 (2011) 3941–3994.
- [13] A. Isogai, T. Saito, H. Fukuzumi, TEMPO-oxidized cellulose nanofiber, *Nanoscale*. 3 (2011) 71–85.
- [14] A. Isogai, Wood nanocelluloses: fundamentals and applications as new bio-based nanomaterials, *J. Wood Sci.* 59 (2013) 449–459.
- [15] Y. Habibi, L.A. Lucia, O.J. Rojas, Cellulose nanocrystals: chemistry, self-assembly, and applications, *Chem. Rev.* 110 (2010) 3479–3500.
- [16] H.Y. Yu, G.Y. Chen, Y.B. Wang, J.M. Yao, A facile one-pot route for preparing cellulose nanocrystal/zinc oxide nanohybrids with high antibacterial and photocatalytic activity, *Cellulose*. 22 (2015) 261–273.
- [17] M. Yadollahi, I. Gholamali, H. Namazi, M. Aghazadeh, Synthesis and characterization of antibacterial carboxymethyl cellulose/ZnO nanocomposite hydrogels, *Int. J. Biol. Macromol.* 74 (2015) 136–141.

- [18] N.C.T. Martins, R. Freire, Carmen S, C.P. Neto, A.J.D. Silvestre, J. Causio, G. Baldi, P. Sadocco, T. Trindade, Antibacterial paper based on composite coatings of nanofibrillated cellulose and ZnO, *Colloids Surfaces A Physicochem. Eng. Asp.* 417 (2013) 111–119.
- [19] E. Lizundia, A. Urruchi, J.L. Vilas, L.M. Leon, Increased functional properties and thermal stability of flexible cellulose nanocrystal/ZnO films, *Carbohydr. Polym.* 136 (2016) 250–258.
- [20] A. John, H.U. Ko, D.G. Kim, J. Kim, Preparation of cellulose-ZnO hybrid films by a wet chemical method and their characterization, *Cellulose*. 18 (2011) 675–680.
- [21] T. Saito, Y. Nishiyama, J. Putaux, M. Vignon, A. Isogai, Homogeneous suspensions of individualized microfibrils from TEMPO-catalyzed oxidation of native cellulose, *Biomacromolecules*. 7 (2006) 1687–1691.
- [22] T. Saito, S. Kimura, Y. Nishiyama, A. Isogai, Cellulose nanofibers prepared by TEMPO-mediated oxidation of native cellulose, *Biomacromolecules*. 8 (2007) 2485–2491.
- [23] H. Fukuzumi, T. Saito, T. Iwata, Y. Kumamoto, A. Isogai, Transparent and high gas barrier films of cellulose nanofibers prepared by TEMPO-mediated oxidation, *Biomacromolecules*. 10 (2009) 162–165.
- [24] R. Shinoda, T. Saito, Y. Okita, A. Isogai, Relationship between length and degree of polymerization of TEMPO-oxidized cellulose nanofibrils, *Biomacromolecules*. 13 (2012) 842–849.
- [25] T. Saito, T. Uematsu, S. Kimura, T. Enomae, A. Isogai, Self-aligned integration of native cellulose nanofibrils towards producing diverse bulk materials, *Soft Matter*. 7 (2011) 8804–8809.
- [26] Y. Okita, T. Saito, A. Isogai, Entire surface oxidation of various cellulose microfibrils by TEMPO-mediated oxidation, *Biomacromolecules*. 11 (2010) 1696–1700.
- [27] I. Sakurada, Y. Nukushina, T. Ito, Experimental determination of the elastic modulus of crystalline regions in oriented polymers, *J. Polym. Sci.* 57 (1962) 651–660.
- [28] C.N. Wu, T. Saito, S. Fujisawa, H. Fukuzumi, A. Isogai, Ultrastrong and high gas-barrier nanocellulose/clay-layered composites, *Biomacromolecules*. 13 (2012) 1927–1932.
- [29] C.N. Wu, Q. Yang, M. Takeuchi, T. Saito, A. Isogai, Highly tough and transparent layered composites of nanocellulose and synthetic silicate, 6 (2014) 392–399.
- [30] M. Bagheri, S. Rabieh, Preparation and characterization of cellulose-ZnO nanocomposite based on ionic liquid ([C<sub>4</sub>mim]Cl), *Cellulose*. 20 (2013) 699–705.
- [31] R.P. Sinha, D.P. Häder, UV-induced DNA damage and repair : a review, *Photochem. Photobiol. Sci.* 1 (2002) 225–236.
- [32] M. Singh, M. Singh, Thermal expansion in zinc oxide nanomaterials, *Nanosci Nanotechnol Res.* 1 (2013) 27–29.
- [33] L.C. Sim, S.R. Ramanan, H. Ismail, K.N. Seetharamu, T.J. Goh, Thermal characterization of Al<sub>2</sub>O<sub>3</sub> and ZnO reinforced silicone rubber as thermal pads for heat dissipation purposes, *Thermochim. Acta*. 430 (2005) 155–165.
- [34] B. Yates, R.F. Cooper, Low-temperature thermal expansion of zinc oxide. Vibrations in zinc oxide and sphalerite zinc sulfide, *Phys. Rev. B*. 4 (1971) 1314–1323.
- [35] D.P. Norton, Y.W. Heo, M.P. Ivill, K. Ip, S.J. Pearton, M.F. Chisholm, T. Steiner, ZnO: growth, doping & processing, *Materialstoday*. 7 (2004) 34–40.
- [36] A.B.D. Cassie, S. Baxter, Wettability of porous surfaces, *Trans. Faraday Soc.* 40 (1944) 546–551.

- [37] E. Hosono, S. Fujihara, I. Honma, H. Zhou, Superhydrophobic perpendicular nanopin film by the bottom-up process, *JACS*. 127 (2005) 13458–13459.
- [38] C.N. Wu, T. Saito, Q. Yang, H. Fukuzumi, A. Isogai, Increase in the water contact angle of composite film surfaces caused by the assembly of hydrophilic nanocellulose fibrils and nanoclay platelets, *ACS Appl. Mater. Interfaces*. 6 (2014) 12707–12712.
- [39] M. Henriksson, L.A. Berglund, P. Isaksson, T. Lindström, T. Nishino, Cellulose nanopaper structures of high toughness, *Biomacromolecules*. 9 (2008) 1579–1585.
- [40] W.C.J. Zuiderduin, C. Westzaan, J. Huétink, R.J. Gaymans, Toughening of polypropylene with calcium carbonate particles, *Polymer*. 44 (2003) 261–275.
- [41] A. Mardilovich, E. Kokkoli, Patterned biomimetic membranes : effect of concentration and pH, *Langmuir*. 21 (2005) 7468–7475.
- [42] M. Harris, G. Appel, H. Ade, Surface morphology of annealed polystyrene and poly(methyl methacrylate) thin film blends and bilayers, *Macromolecules*. 36 (2003) 3307–3314.

## **Chapter 3**

# **Influences of the morphology of ZnO nanoparticles on films properties of ZnO/TOCN composites**

### **3.1 Abstract**

ZnO nanoparticles with different morphologies, including spheres, rods, and needles, and TOCNs were mixed in water and then cast and dried to give ZnO/TOCN (1:9 w/w) composite films to investigate the influence of ZnO nanoparticle morphology on composite film properties. TOCNs were used as the matrix of ZnO-containing composite films because TOCN films have high transparencies. The film densities varied from 1.25 to 1.63 g/cm<sup>3</sup> and porosities ranged from 5.4 to 22 vol%, depending on the ZnO nanoparticle morphology. The (100) plane of the rod- and needle-like wurtzite ZnO particles were preferentially oriented to the composite film surfaces. The Young's modulus and tensile strength of the composite films were similar regardless of nanoparticle morphology, whereas the ZnO/TOCN films with higher porosities had greater elongations at break and works of fracture. The composite films with rod- and needle-like ZnO particles had low oxygen permeability at 50% relative humidity. All the ZnO/TOCN composite films screened UV light, and the film with spherical ZnO nanoparticles had the highest visible-light transmittance. The ZnO/TOCN composite films and their components showed photoluminescence when excited by UV light with the highest intensity at 370-nm UV light. The composite films in aqueous methylene blue (MB) solution under UV irradiation restricted the UV-induced ZnO-catalyzed degradation of MB.

### **3.2 Introduction**

In Chapter 2, ZnO/TOCN composite films with various ZnO/TOCN weight ratios were prepared using spherical ZnO nanoparticles by mixing ZnO and TOCNs in water and subsequent casting and drying the ZnO/TOCN aqueous dispersions. The optical, thermal, hydrophilic/hydrophobic, and mechanical properties of these composite films were investigated in terms of their ZnO content. The porosity of the composite films increased with ZnO content. The aggregation of cationic ZnO particles and anionic TOCN may have caused the formation of porous structures in the ZnO/TOCN composite

films. The ZnO/TOCN composite film with a ZnO/TOCN weight ratio of 1:9 displayed high visible light transparency as well as UV screening properties. The ZnO/TOCN composite films had low CTEs, although their CTE values did increase with ZnO content.

Because ZnO particles have unique optical properties and UV-induced catalytic activities, that depend on their morphology [1,2], the properties of ZnO/TOCN composite films may be affected by the morphology of the ZnO nanoparticles [3–5]. However, the influence of the morphology of ZnO nanoparticles on the properties of ZnO/TOCN composite films has not been investigated.

In this chapter, ZnO/TOCN composite films containing ZnO nanoparticles with different morphologies are prepared by casting and drying aqueous ZnO/TOCN mixtures. The porous, hydrophilic, thermal, mechanical, optical, and oxygen barrier properties of the ZnO/TOCN composite films as well as their XRD patterns are investigated to determine the effect of ZnO morphology on the composite properties. Moreover, the UV-induced catalytic degradation behavior of methylene blue (MB:  $C_{16}H_{18}ClN_3S$ , Figure 3A.1 in the Appendix) dissolved in water in the presence of TOCN and ZnO/TOCN films is studied to characterize the effect of the ZnO/TOCN composite films on the degradation behavior of MB.

## 3.3 Materials and methods

### 3.3.1 Materials

Never-dried softwood bleached kraft pulp was supplied by Nippon Paper (Tokyo, Japan) and used as wood cellulose. TEMPO, ZnO particles with spherical, rod-like, and two needle-like morphologies (denoted as ZnO-S, ZnO-R, ZnO-N1, and ZnO-N2, respectively) were purchased from Sigma-Aldrich (USA). MB (98.5%, Tianjin Chemical Reagent Co., Ltd. Tianjin, China) was used in UV-induced catalytic degradation measurements. Sodium bromide, 2 M sodium hypochlorite solution, sodium hydroxide, sodium borohydride ( $NaBH_4$ ), and other reagents were of laboratory grade and used as received from Wako Pure Chemicals (Tokyo, Japan). TEMPO-oxidized cellulose (TOC) subjected to post reduction with  $NaBH_4$  was prepared from the wood cellulose according to previously reported methods [6,7]. The TOC with a sodium carboxylate content of 1.35 mmol/g was suspended in water to give a 0.4% TOC content and then mechanically disintegrated using a high-pressure homogenizer (Star Burst Labo HJP-25005×; Sugio Machine Limited, Toyama, Japan) at 150 MPa for five passes. The

small unfibrillated fraction was removed by centrifugation at 12000 ×g for 15 min to obtain transparent TOCN/water dispersions. The TOCN concentration was adjusted to 0.4% (w/v) by partial removal of water using a rotary evaporator at 40 °C.

### **3.3.2 Preparation of ZnO/TOCN nanocomposite films**

Each type of ZnO particle was suspended in water at a concentration of 2% (w/v), and then the suspensions were sonicated for 1 h in an ultrasonic bath (M1800-J; Yamato Scientific, Tokyo, Japan). The ZnO/water dispersion (2% w/v, 0.22 mL) was added to the TOCN dispersion (0.4% w/v, 10 mL) to give a ZnO:TOCN weight ratio of 1:9. The mixture was agitated using a vortex for 30 s and then sonicated in an ultrasonic homogenizer (US-300E; Nihon Seiki, Tokyo, Japan) for 30 s. The vortex and ultrasonic treatments were repeated twice. The obtained ZnO/TOCN aqueous dispersion was poured into a Petri dish with a diameter of 50 mm and then dried in an oven at 40 °C for 24 h. The resulting ZnO/TOCN composite film was carefully peeled off the dish and then placed in a conditioning room at 23 °C and 50% RH. The ZnO/TOCN composite films prepared with ZnO-S, ZnO-R, ZnO-N1, and ZnO-N2 ZnO particles are referred to as ZnO-S/TOCN, ZnO-R/TOCN, ZnO-N1/TOCN, and ZnO-N2/TOCN, respectively. The water contents of the films at 23 °C and 50% RH were calculated from their weights before and after drying at 105 °C for 3 h. The densities and porosities of the films at 23 °C and 50% RH were calculated from their volumes at 23 °C and 50% RH and dry weights.

### **3.3.3 Characterization of ZnO particles and ZnO/TOCN composite films**

Average sizes and  $\zeta$ -potentials of ZnO particles were measured in water using a particle size analyzer (Delsa Nano HC, Beckman Coulter, Germany). Scanning electron microscopy (SEM) observation of ZnO particles and ZnO/TOCN composite film surfaces was performed using a field-emission microscopy (Hitachi S4800, Tokyo, Japan) at acceleration voltages of 1.0 kV. The ZnO/TOCN film surfaces were coated using a carbon coater (CC-40-F, Meiwa Shoji, Co., Japan) before SEM observation. XRD patterns of ZnO particles and ZnO/TOCN composite films were obtained using a diffractometer (Rigaku RINT 2000, Tokyo, Japan) with monochromatized Cu K $\alpha$  radiation ( $\lambda = 0.15418$  nm) at 40 mV and 40 mA. Ultraviolet-visible (UV-vis) transmittance spectra and photoluminescence spectra following excitation at 370 nm were obtained for the ZnO/TOCN composite films using a V-670 UV-Vis spectrophotometer (JASCO, Japan) and FP-8500 fluorescence



spectrometer (JASCO, Japan), respectively. Water contact angles on the film surfaces were measured using a contact angle apparatus (Kyowa FAMAS DM500; Saitama, Japan) at 23 °C and 50% RH. Tensile tests were performed using a tensile tester (Shimadzu EZ-TEST, Kyoto, Japan) equipped with a 500-N load cell at 23 °C and 50% RH. Rectangular specimens with dimensions of 20 × 2 mm were measured at a crosshead speed of 1.0 mm/min with a 10-mm span length.

### **3.3.4 UV-induced catalytic degradation of MB in water**

A ZnO/TOCN composite film (30 mg) was added to water (30 mL) containing MB (0.3 mg) in a tube of a photochemical reaction system (TOPT-V; Toption Instrument Co., Ltd., Xi'an, China). A total of eight tubes were set in the reaction system. The mixture in each tube was stirred with a magnetic stirring bar in the dark for 1 h. During stirring, the ZnO/TOCN film was partly disintegrated to ZnO particles and TOCN fragments dispersed in the mixture. UV light was then irradiated onto the continuously stirred mixtures using a high-pressure mercury lamp with the highest intensity at 365 nm (500 W) set in the photochemical reaction system. Every 20 min after starting the UV irradiation, one tube was taken from the system and then the mixture was immediately subjected to centrifugation at 16000 ×g for 10 min to remove ZnO particles and TOCN fragments. The absorbance of the supernatant was measured using a UV-vis spectrophotometer (U-3900; Hitachi, Japan). The degree of MB degradation was calculated from change in light absorption of the supernatant at 665 nm.

## **3.4 Results and discussion**

### **3.4.1 Fundamental properties**

SEM images of the ZnO particles are shown in [Figure 3A.2](#), and their average particle sizes and  $\zeta$ -potentials are listed in [Table 3.1](#). The ZnO-S particles had spherical morphology, whereas the ZnO-R particles had rod-like morphology. The ZnO-N1 and ZnO-N2 particles had needle-like morphologies with high aspect ratios. All the ZnO particles had positive surface charges ranging from +21 to +29 mV in water, and the average particle sizes increased in the order of ZnO-S < ZnO-R < ZnO-N1 < ZnO-N2, which is consistent with the catalog data provided by the manufacturer (Sigma-Aldrich).

**Table 3.1.** Characteristics of the ZnO particles used in this study.

ZnO sample	Average width <sup>a</sup> (nm)	Average length <sup>a</sup> (nm)	Aspect ratio <sup>a</sup>	ζ-Potentials <sup>b</sup> (mV)	Average particle size <sup>b</sup> (nm)	Polydispersity index <sup>b</sup>
ZnO-S	35	35	1	+28.5	66	0.22
ZnO-R	50	300	6	+22.2	420	0.32
ZnO-N1	90	1000	11	+20.4	1760	0.44
ZnO-N2	300	4000-5000	13-17	+24.0	1900	0.42

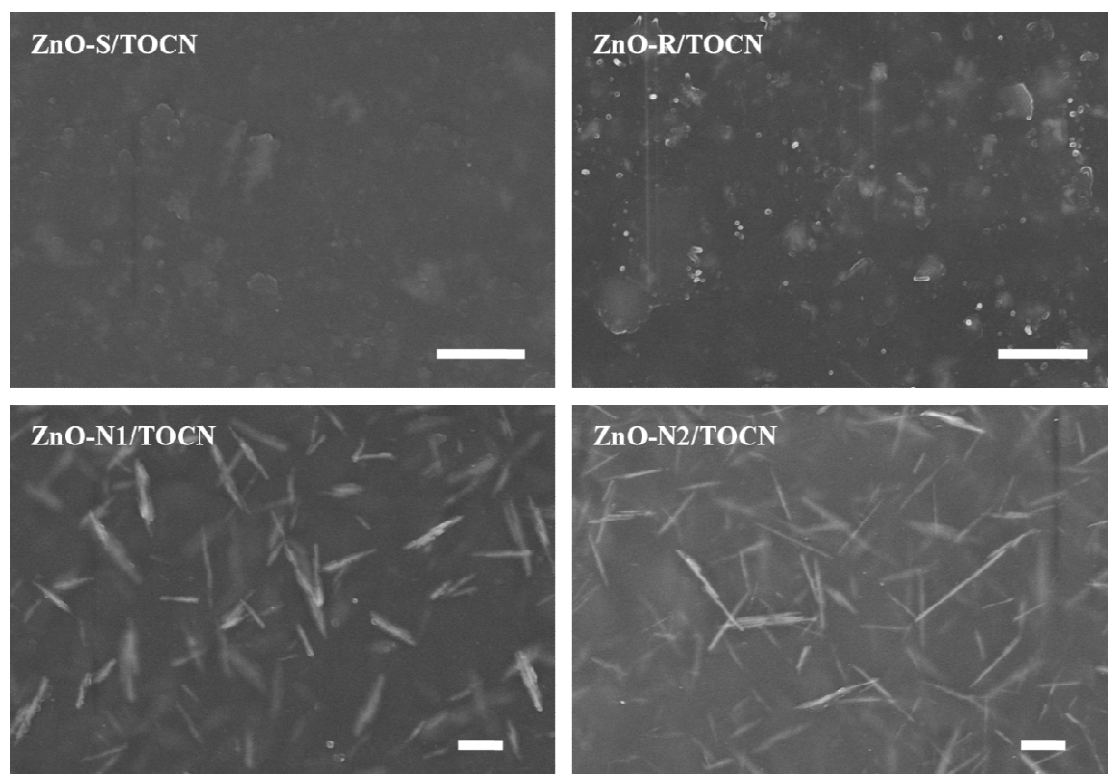
<sup>a</sup> Catalog data.<sup>b</sup> Measured using a particle analyzer.**Figure 3.1.** SEM images of ZnO/TOCN (1:9 w/w) composite film surfaces. (Scale bar = 2  $\mu$ m)

Figure 3.1 shows SEM images of the ZnO/TOCN composite film surfaces. The ZnO-S particles could not be observed on the film surface at the magnification level used, indicating that the ZnO-S particles were almost homogeneously dispersed in the film and did not form aggregates. In contrast, the rod-like ZnO-R and needle-like ZnO-N1 and ZnO-N2 particles were clearly observed as bright spots

on the surface of the dark TOCN matrix. This indicates that some of the ZnO particles were present as aggregates in the films, showing that complete dispersion of the ZnO particles in water and in the TOCN matrix is difficult to achieve.

**Table 3.2.** Calculated and measured film densities, water contents, and porosities of neat TOCN and ZnO/TOCN composite films conditioned at 23 °C and 50% RH.

Film sample	Calculated film density <sup>a</sup> (g/cm <sup>3</sup> )	Measured film density <sup>b</sup> (g/cm <sup>3</sup> )	Water content (wt%)	Porosity <sup>c</sup> (vol%)
Neat TOCN	1.60	1.53	7.3	4.4
ZnO-S/TOCN	1.72	1.63	10.0	5.4
ZnO-R/TOCN	1.72	1.37	9.2	21
ZnO-N1/TOCN	1.72	1.46	9.5	15
ZnO-N2/TOCN	1.72	1.35	9.2	22

<sup>a</sup> Calculated from the densities of a pure ZnO wurtzite crystal (5.6 g/cm<sup>3</sup>) and cellulose I crystal (1.6 g/cm<sup>3</sup>) and the ZnO/TOCN weight ratio of 1:9 assuming zero pore volume.

<sup>b</sup> Measured from the weight and size of films

<sup>c</sup> Calculated from the measured densities of films

All the composite films had similar average thicknesses of 12–14 μm. The film densities, water contents, and porosities of the ZnO/TOCN composite films at 23 °C and 50% RH are listed in Table 3.2. When the film densities were calculated from those of pure crystalline cellulose I and ZnO wurtzite crystal of 1.6 and 5.6 g/cm<sup>3</sup>, respectively [8,9], and it was assumed that no pores were present in the films, all the ZnO/TOCN composite films with a 1:9 weight ratio had densities of 1.72 g/cm<sup>3</sup>. The neat TOCN and ZnO-S/TOCN composite films had measured film densities of 1.53 and 1.63 g/cm<sup>3</sup>, respectively, indicating that some pores were present in these films. The porosities of these films were calculated to be 4.4 and 5.4 vol%, respectively. The densities of the ZnO-S/TOCN, ZnO-N1/TOCN, and ZnO-N2/TOCN composite films were much lower than the calculated value, and these films had porosities of 15–22 vol%. All the ZnO/TOCN composite films had water contents of 9.2%–10%, which

were higher than that of the neat TOCN film (7.3%). This is likely because the ZnO particle surfaces are hydrophilic and attract water into the film.

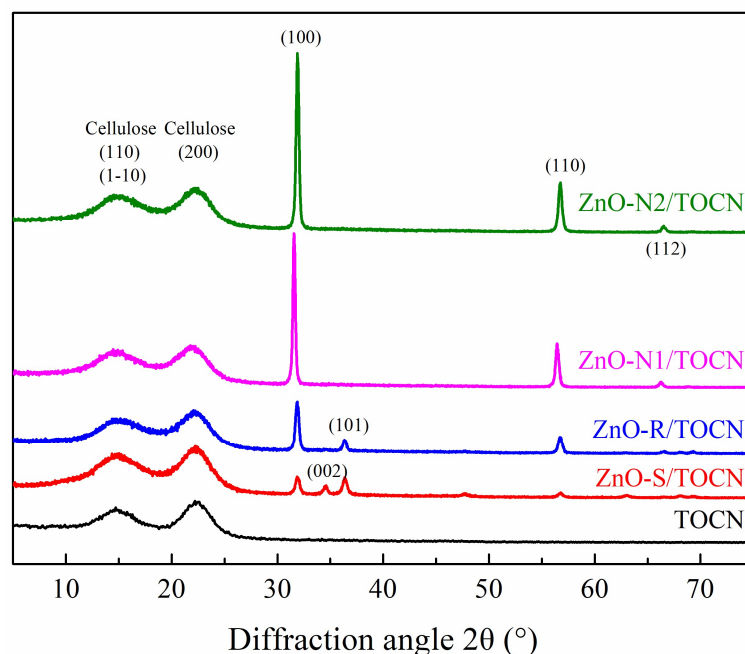
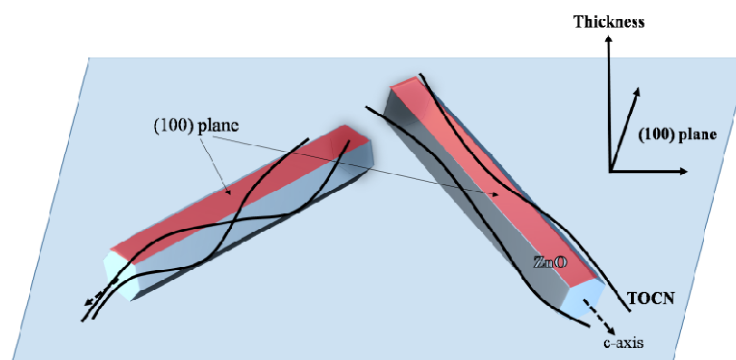


**Figure 3.2.** XRD patterns of TOCN film and ZnO/TOCN composite films.



**Schematic 3.1.** Preferred-orientation of (100) plane of ZnO wurtzite crystals in ZnO/TOCN composite films.

The XRD patterns of the original ZnO particles are presented in Figure 3A.3. All the ZnO particles were composed of typical hexagonal wurtzite crystals [10]. The XRD patterns of the ZnO/TOCN composite films are shown in Figure 3.2. The ZnO-S/TOCN film had a simple XRD pattern consisting of the superposition of the original XRD patterns of TOCNs and ZnO-S. In contrast,

the ZnO-R/TOCN, ZnO-N1/TOCN, and ZnO-N2/TOCN composite films showed clear orientation of the (100) plane of the ZnO wurtzite crystals parallel to the film surface (Schematic 3.1). Similar orientation behavior of the (100) plane of ZnO was also observed for ZnO-N2/poly(vinyl alcohol), ZnO-N2/carboxymethylcellulose, and ZnO-N2/microfibrillated cellulose (MFC) films (MFC was mechanically fibrillated cellulose prepared from wood cellulose, “Celish®” provided by Daicel, Tokyo, Japan) (Figure 3A.4). Because the orientation degree of the (100) plane in the composite films increased with the ZnO particle size, i.e., with the order of ZnO-N2 > ZnO-N1 > ZnO-R, the aggregation behavior of needle-like ZnO particles in the films may have primarily led to the results in Figure 3.2.

### 3.4.2 Thermal and mechanical properties

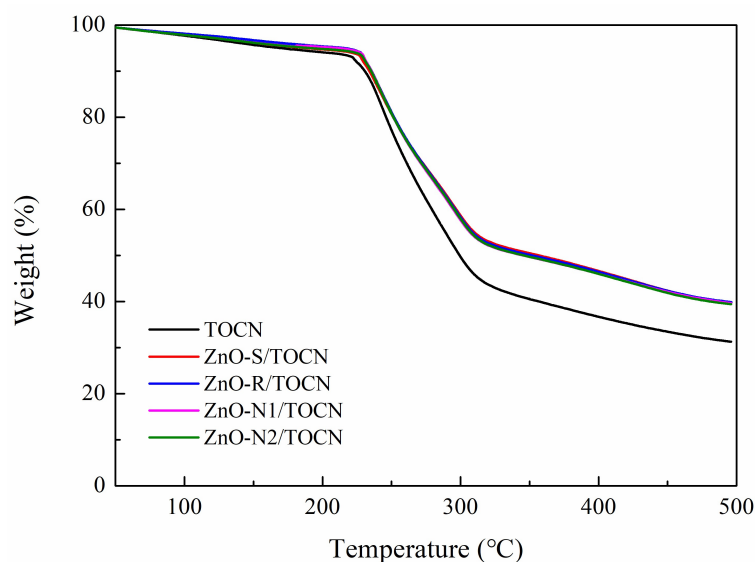


**Figure 3.3.** Thermogravimetric curves of neat TOCN and ZnO/TOCN composite films.

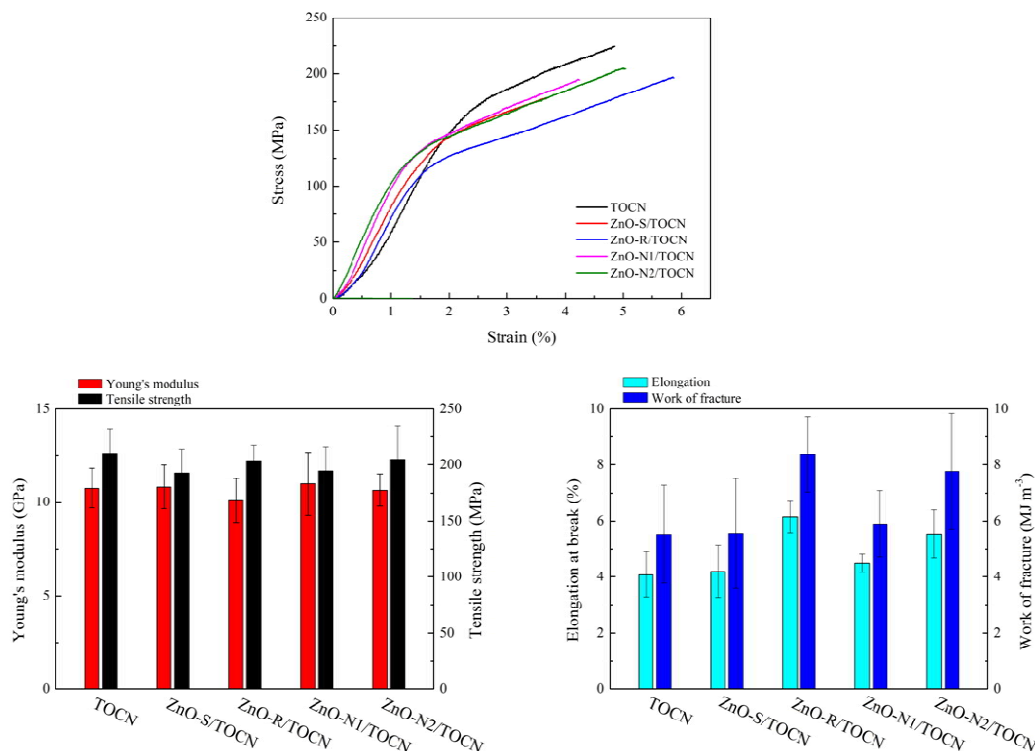


**Figure 3.4.** Typical strain-stress curves and mechanical properties of neat TOCN and ZnO/TOCN composite films.

Thermogravimetric curves and mechanical properties of neat TOCN and ZnO/TOCN composite films are presented in Figures 3.3 and 3.4, respectively. The presence of ZnO particles did not clearly improve the thermal stability of TOCNs, which degraded  $\sim 220$  °C [11]. However, the temperatures at 5% weight loss in the thermogravimetric curves increased slightly from 170 °C for the neat TOCN film to 190–220 °C for the ZnO/TOCN composite films. These increases in 5% weight loss temperature may have been caused by the presence of thermally stable ZnO particles in the films based on our previous results (Chapter 2) and those reported for polyoxymethylene/ZnO composites [12]. The presence of 10 wt% ZnO particles with different morphologies in the composite films did not strongly affect the Young's modulus or tensile strength of the composite films. However, the ZnO-R/TOCN and ZnO-N2/TOCN films had elongations at break and works of fracture that were greater than those of the other films. Because these two films had porosities of 20–21 vol%, which were higher than those of the other films, the porous structures of the ZnO-R/TOCN and ZnO-N2/TOCN films may have caused the greater elongations at break [13–15], resulting in the higher works of fractures. The porous structures of the ZnO-R/TOCN and ZnO-N2/TOCN films may have been caused by the aggregation behavior of

the ZnO particles in these composite films.

### 3.4.3 Hydrophilicity and oxygen permeability

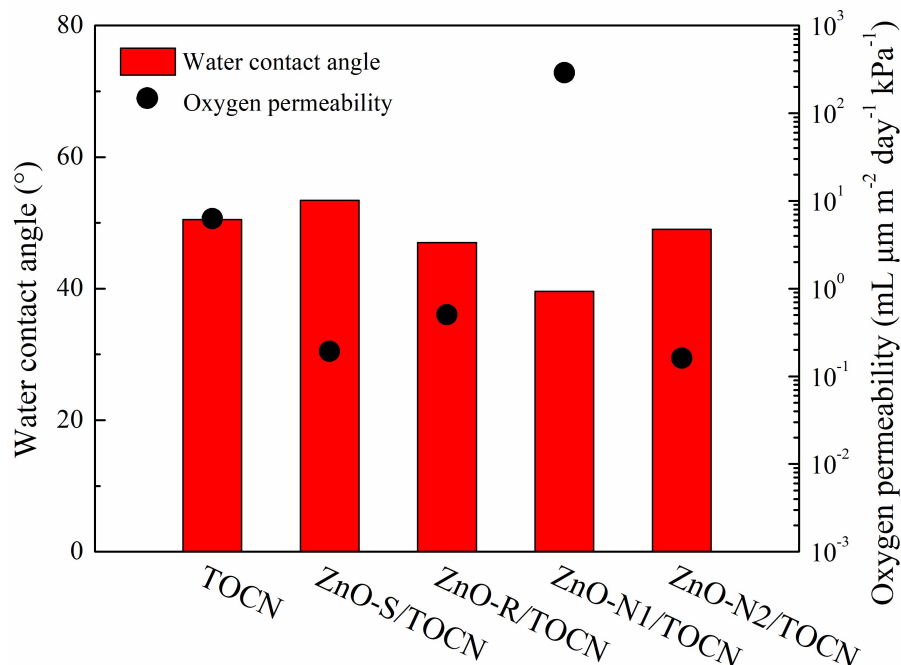


**Figure 3.5.** Water contact angles and oxygen permeability at 50% RH of neat TOCN and ZnO/TOCN composite films.

The water contact angles and oxygen permeability at 50% RH of the neat TOCN and ZnO/TOCN composite films are presented in [Figure 3.5](#). The hydrophilic nature of the TOCN film did not markedly change in the ZnO/TOCN composite films according to the measured water contact angles. Water contact angle is also influenced by the surface roughness of a film. However, all the films had smooth surfaces on the side attached to the Petri dish during the film preparation process. One of the disadvantages of TOCN films is their remarkable increase in oxygen permeability (or decrease in oxygen barrier properties) at high RH, even though TOCN films have extremely low oxygen permeabilities under dry conditions [\[16\]](#). The hydrophilic nature of TOCN films is caused by the abundant sodium carboxylate groups present in TOCNs. As shown in [Figure 3.5](#), the oxygen permeability of the films decreased considerably from  $\sim 10 \text{ mL } \mu\text{m}^{-2} \text{day}^{-1} \text{kPa}^{-1}$  for the TOCN film to  $\sim 0.1 \text{ mL } \mu\text{m}^{-2} \text{day}^{-1} \text{kPa}^{-1}$  for the ZnO-S/TOCN and ZnO-N2/TOCN composite films. When crystalline nanoparticles are incorporated into a polymer matrix as fillers sufficiently dispersed in the

matrix, the oxygen permeability of filler/polymer composite films effectively decreases, depending on the volume fractions and aspect ratios of the fillers in films [17,18]. The low oxygen permeability of ZnO/TOCN composite films can be explained in terms of the same mechanism. The ZnO-N1/TOCN film has high oxygen permeability different from other ZnO/TOCN films, probably because the ZnO-N1 particles strongly aggregated in the composite film. Details are discussed in the following section.

### 3.4.4 Optical properties

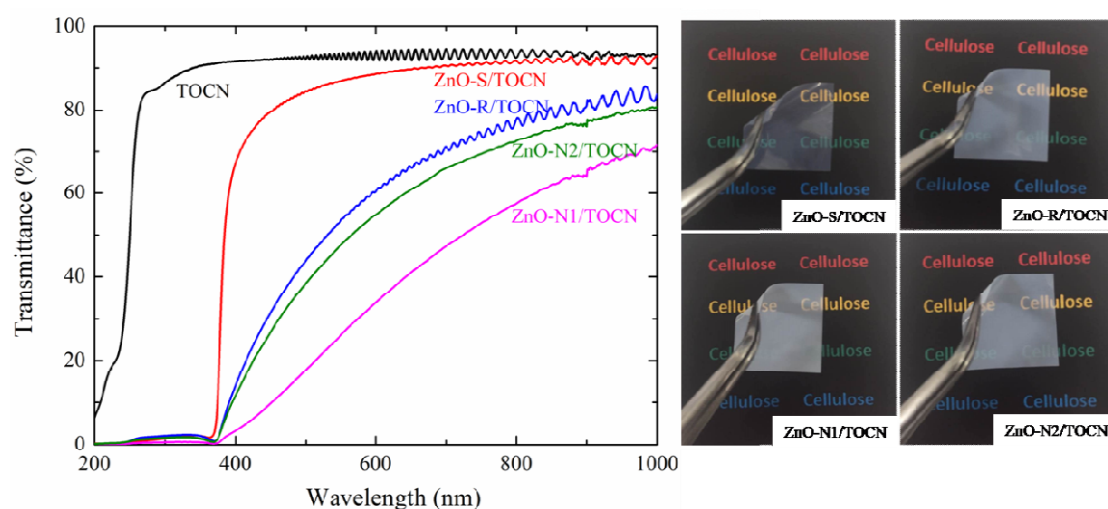


**Figure 3.6.** UV-vis transmittance spectra of ZnO/TOCN composite films with a normalized film thickness of 10  $\mu\text{m}$  and photographs of the four representative composite films.

Figure 3.6 shows UV-vis transmittance spectra and photographs of the films. All of the ZnO/TOCN composite films completely screened UV light with wavelength shorter than 380 nm. The ZnO-S/TOCN composite film had a high visible-light transmittance of  $\sim 90\%$  at 600 nm, whereas the other ZnO/TOCN composite films had lower transmittances with increasing ZnO particle size. The ZnO-N1/TOCN film had the lowest visible light transmittance of the composite films, indicating that the ZnO-N1 particles formed aggregates in the film, which was also indicated by its high oxygen permeability (see Figure 3.5).

ZnO particles display photoluminescence caused by molecular defects in the ZnO crystals [19–22], which behave as active sites of UV-induced catalytic reactions. Figure 3A.5 reveals that the ZnO particles had two predominant photoluminescence peaks; ZnO-S displayed weak peaks at  $\sim 425$



and ~554 nm, ZnO-R exhibited intense peaks at ~392 and ~554 nm, and ZnO-N1 and ZnO-N2 showed intense peaks at ~392 and 550 nm [21].

The neat TOCN film showed visible photoluminescence at ~428 nm, as reported previously [23–25], although the origin of photoluminescence from cellulose samples has not been identified. The ZnO/TOCN composite films showed UV and green emission bands from the ZnO particles, and a weak peak originating from TOCNs. The UV emission peak of ZnO blue-shifted slightly from ~392 nm for the ZnO particles to ~380 nm for the ZnO/TOCN films. Thus, the TOCNs influenced the UV emission peak position of the ZnO particles.

### 3.4.5 UV and ZnO-induced catalytic degradation of MB

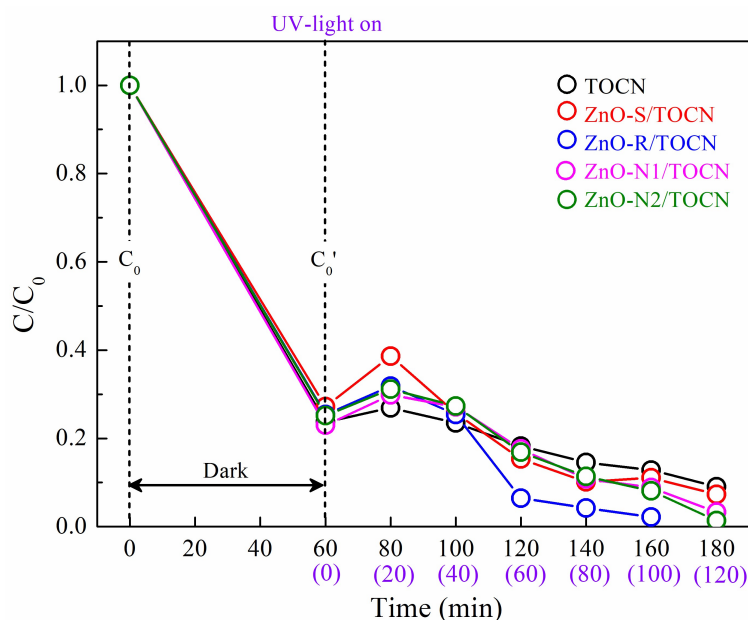


**Figure 3.7.** Relative changes of the light absorption of MB at 665 nm in the presence of a TOCN or ZnO/TOCN film at the initial state ( $C_0$ ), after stirring the mixture in the dark for 60 min ( $C_0'$ ), and during UV irradiation at 365 nm for up to 120 min.

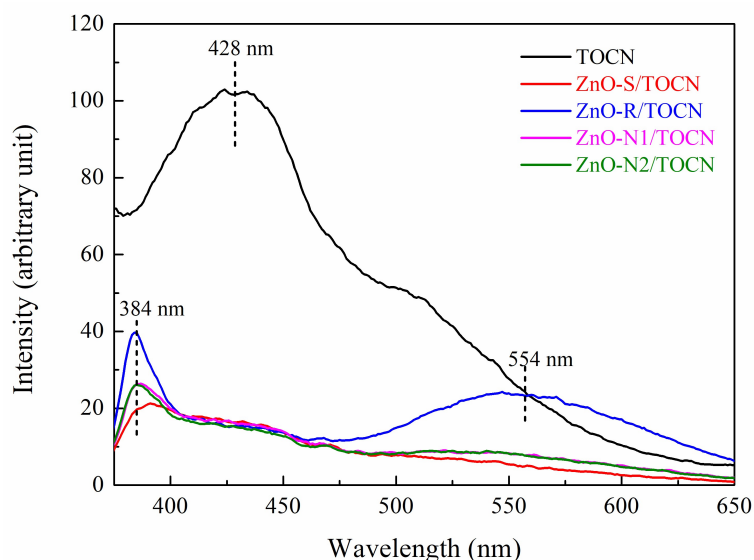


**Figure 3.8.** Photoluminescence spectra of neat TOCN and ZnO/TOCN composite films obtained at an excitation wavelength of 370 nm.

The degradation behavior of MB using the TOCN and ZnO/TOCN composite films under UV light was investigated because ZnO wurtzite particles possess photocatalytic activity (Figure 3A.5). The original TOCN film form was mostly destroyed and dispersed as small fragments in water after stirring in water for 1 h in the dark (Figure 3A.6). The absorption spectrum of the initial aqueous MB solution contained two peaks at ~614 and ~665 nm [26,27]. Changes in the light absorption of MB during UV irradiation with the highest intensity at 365 nm under various conditions are presented in Figure 3A.7. The original light absorption intensity and corresponding absorption spectrum of MB in water were unchanged in the dark. During UV exposure, the absorption intensity of MB in water gradually decreased over time. When the ZnO-S particles were present, the absorption of MB almost disappeared after UV irradiation for 20 min. The absorption of MB almost disappeared within 100 min of UV irradiation in the presence of the other ZnO particles. These results demonstrate that all the ZnO particles displayed UV-induced degradation activity towards MB. When the TOCN film without ZnO was present in the MB aqueous solution, the original absorption intensity of MB decreased considerably even in the dark without UV irradiation and a new absorption peak appeared at ~578 nm given by the trimer structure of MB molecules [26,27]. Then, the absorption of MB at 665 nm gradually decreased with lengthening UV irradiation time. Because TOCN fragments formed through the disintegration of the TOCN film in water have negative surface charges originating from their

abundant sodium carboxylate groups, some of the cationic BM molecules may have adsorbed on the anionic TOCN fragments present in the mixture through electrostatic interactions. This is the reason why the MB absorption intensity at 665 nm decreased in the presence of TOCN in the dark. The changes in the light absorption spectrum of MB in the presence of the ZnO/TOCN films were similar to those observed for the TOCN film. It is therefore likely that the presence of anionic TOCN fragments in the mixture restricted the ZnO-catalyzed photodegradation of MB [27]. The degradation of MB in water in the presence of the TOCN and ZnO/TOCN composite films was monitored using the changes in the absorption intensity at 665 nm of the mixtures in the dark and during UV irradiation (Figure 3.7). The neat TOCN film displayed photoluminescence when irradiated by UV light with the highest intensity at 365 nm (Figure 3.8), indicating that the TOCN fragments should have the capability to induce photodegradation of MB. However, the clear decrease in the absorption of MB at 665 nm occurred even in the dark. Moreover, the degradation of MB in the presence of TOCNs during UV irradiation was not enhanced markedly, compared with that in the presence of ZnO-S particles alone (Figure 3A.7b).

### 3.5 Conclusions

ZnO/TOCN (1:9 w/w) composite films containing ZnO particles with different morphologies were prepared by mixing aqueous ZnO particle dispersions with TOCN dispersions, which were then cast and dried. The ZnO-R/TOCN, ZnO-N1/TOCN, and ZnO-N2/TOCN composite films had high porosities of 15–22 vol%, indicating that some ZnO particles formed aggregates in the composite films. The (100) plane of the rod- and needle-like wurtzite ZnO particles was preferentially oriented in the films, whereas no such crystal plane orientation was observed for the ZnO-S/TOCN film containing spherical ZnO particles. The ZnO-R/TOCN, ZnO-N1/TOCN, and ZnO-N2/TOCN composite films had large elongations at break and correspondingly large works of fracture, whereas the Young's modulus, tensile strength, and thermal degradation points of the neat TOCN and ZnO/TOCN composite films were almost the same. The ZnO-S/TOCN and ZnO-N1/TOCN films exhibited higher oxygen barrier properties at 50% RH compared with those of the TOCN film, even though the water contact angles on the film surfaces were similar. All the ZnO/TOCN composite films screened UV light, and the ZnO-S/TOCN film had the highest visible-light transmittance of the films. The neat TOCN film

exhibited photoluminescence at ~428 nm, although this behavior probably did not contribute to the photodegradation of MB. The photoluminescence of TOCNs almost disappeared when the ZnO particles were present in the TOCN matrix. The photocatalytic degradation of MB by ZnO particles was restricted in the aqueous MB/ZnO/TOCN mixtures under UV irradiation because of electrostatic interactions between anionic TOCN fragments and cationic MB molecules.

### 3.6 Appendix

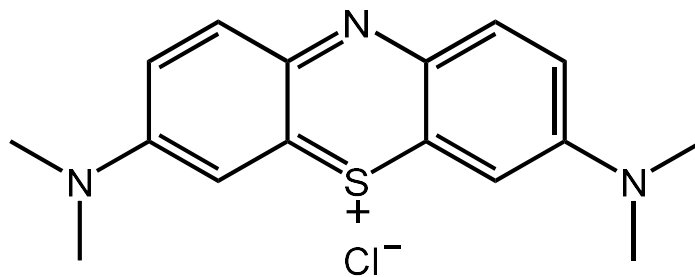


**Figure 3A.1.** Chemical structure of methylene blue (MB).

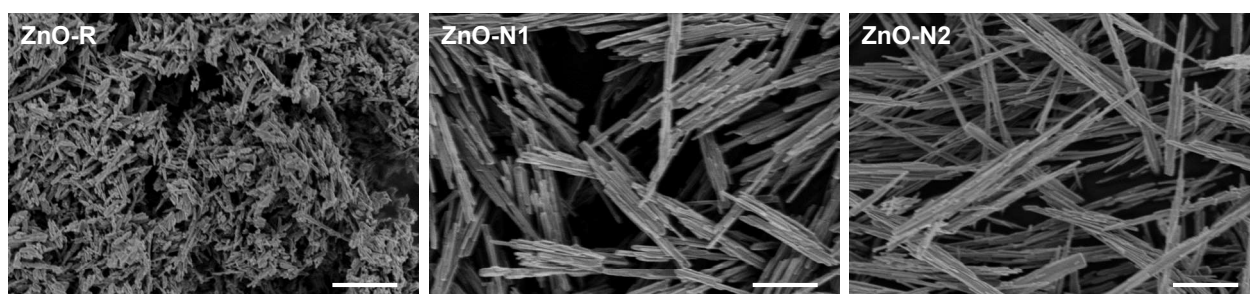


**Figure 3A.2.** SEM images of ZnO-R, ZnO-N1, and ZnO-N2 particles. (Scale bar = 2  $\mu\text{m}$ )

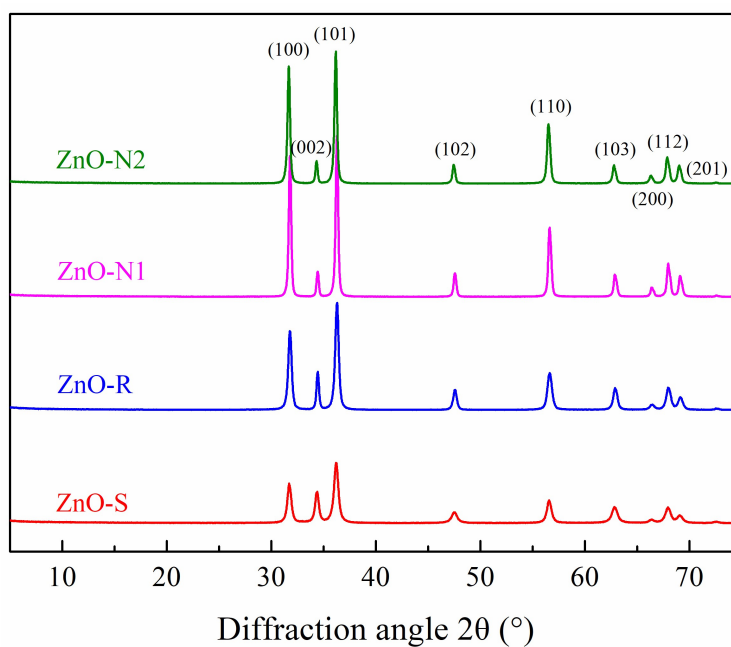


**Figure 3A.3.** XRD patterns of ZnO particles.

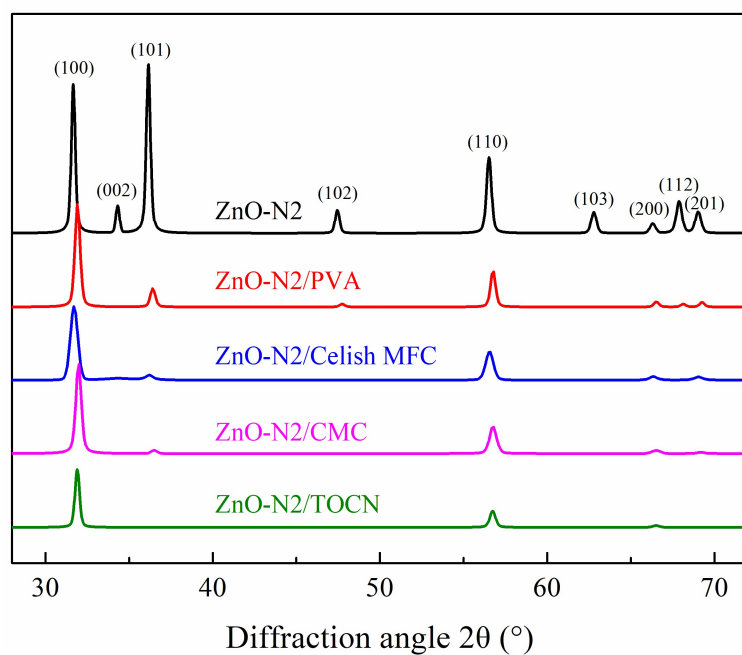


**Figure 3A.4.** XRD patterns of ZnO-N2 particles and composite films of several ZnO-N2/water soluble polymers

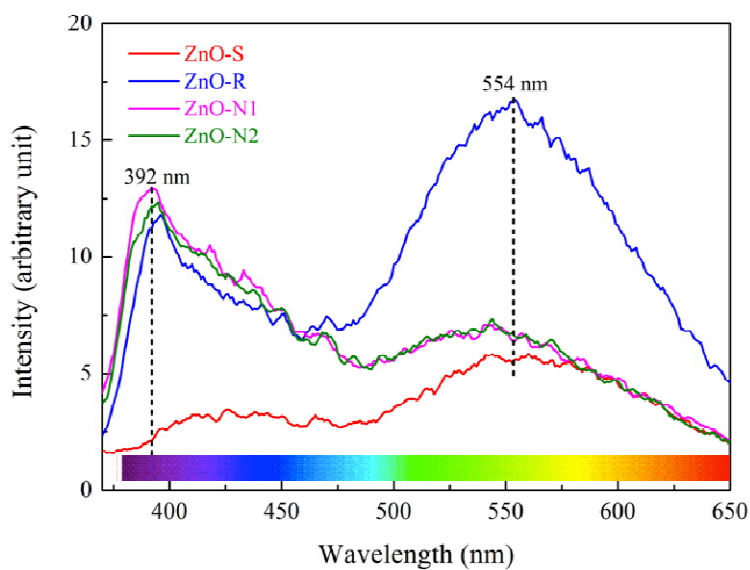


**Figure 3A.5.** Photoluminescence spectra of ZnO particles under UV excitation at 370nm.

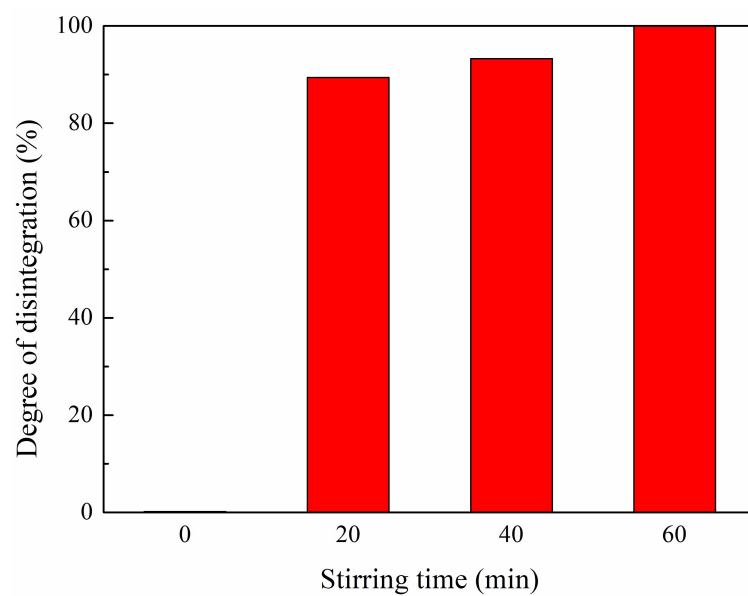


**Figure 3A.6.** Degree of disintegration of TOCN film in water during stirring at 1000 rpm for 20-60 min in the dark.

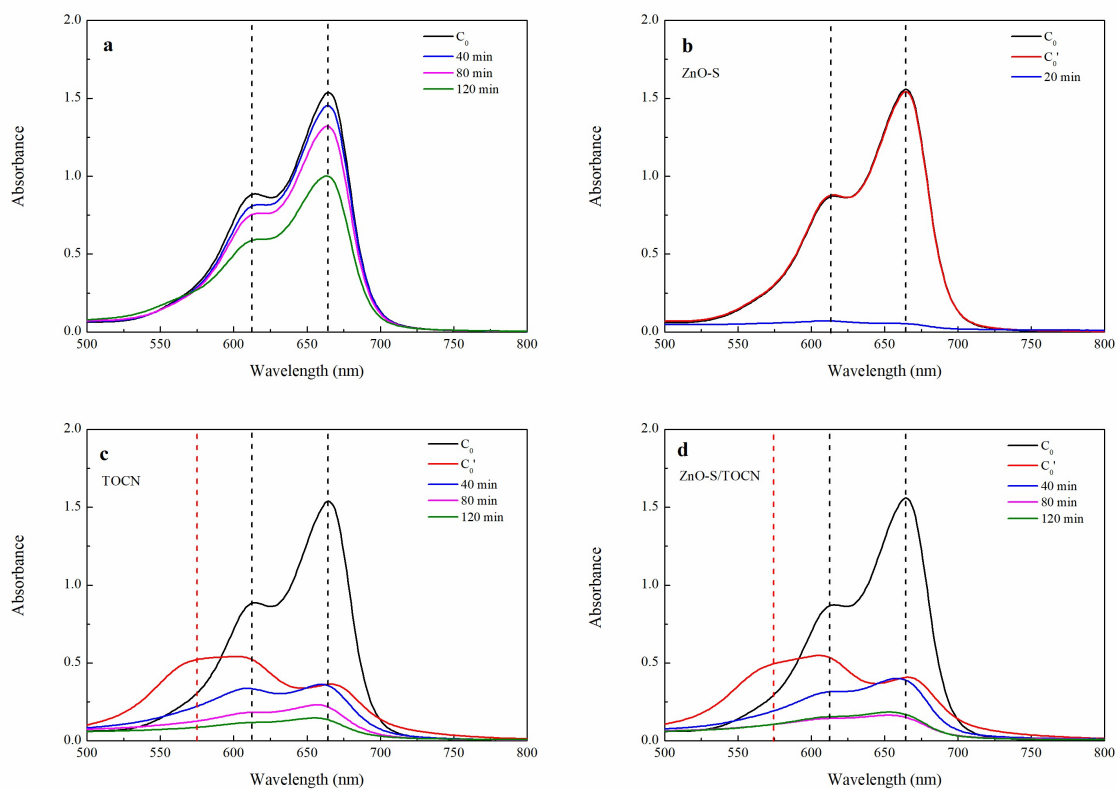


**Figure 3A.7.** Visible light absorption of MB in water at the initial state ( $C_0$ ), 60 min after stirring the mixtures in the dark ( $C_0'$ ), and during 365-nm UV irradiation for up to 120 min. Absorption spectra of (a) MB alone, (b) MB and ZnO-S particles, (c) MB and TOCN film, and (d) MB and ZnO-S/TOCN film.



### 3.7 References

- [1] Ü. Özgür, Y.I. Alivov, C. Liu, A. Teke, M.A. Reshchikov, S. Doğan, V. Avrutin, S.J. Cho, H. Morkoç, A comprehensive review of ZnO materials and devices, *J. Appl. Phys.* 98 (2005) 1–103.
- [2] A. Kolodziejczak-Radzimska, T. Jesionowski, Zinc oxide-From synthesis to application: a review, *Materials*. 7 (2014) 2833–2881.
- [3] M. Tisza, Z. Lukacs, G. Gál, Integrated process simulation and die-design in sheet metal forming, *Int. J. Mater. Form.* 1 (2008) 185–188.
- [4] E. Tang, G. Cheng, X. Ma, Preparation of nano-ZnO/PMMA composite particles via grafting of the copolymer onto the surface of zinc oxide nanoparticles, *Powder Technol.* 161 (2006) 209–214.
- [5] E. Lizundia, A. Urruchi, J.L. Vilas, L.M. León, Increased functional properties and thermal stability of flexible cellulose nanocrystal/ZnO films, *Carbohydr. Polym.* 136 (2016) 250–258.
- [6] S. Takaichi, T. Saito, R. Tanaka, A. Isogai, Improvement of nanodispersibility of oven-dried TEMPO-oxidized celluloses in water, *Cellulose*. 21 (2014) 4093–4103.
- [7] R. Shinoda, T. Saito, Y. Okita, A. Isogai, Relationship between length and degree of polymerization of TEMPO-oxidized cellulose nanofibrils, *Biomacromolecules*. 13 (2012) 842–849.
- [8] I. Sakurada, Y. Nukushina, T. Ito, Experimental determination of the elastic modulus of crystalline regions in oriented polymers, *J. Polym. Sci.* 57 (1962) 651–660.
- [9] D.P. Norton, Y.W. Heo, M.P. Ivill, K. Ip, S.J. Pearton, M.F. Chisholm, T. Steiner, ZnO: growth, doping & processing, *Materialstoday*. 7 (2004) 34–40.
- [10] A.K. Zak, W.H.A. Majid, M.E. Abrishami, R. Yousefi, X-ray analysis of ZnO nanoparticles by Williamson-Hall and size-strain plot methods, *Solid State Sci.* 13 (2011) 251–256.
- [11] H. Fukuzumi, T. Saito, Y. Okita, A. Isogai, Thermal stabilization of TEMPO-oxidized cellulose, *Polym. Degrad. Stab.* 95 (2010) 1502–1508.
- [12] S. Wacharawichanant, S. Thongyai, A. Phutthaphan, C. Eiamsam-ang, Effect of particle sizes of zinc oxide on mechanical, thermal and morphological properties of polyoxymethylene/zinc oxide nanocomposites, *Polym. Test.* 27 (2008) 971–976.
- [13] R. Ning, C.N. Wu, M. Takeuchi, T. Saito, A. Isogai, Preparation and characterization of zinc oxide/TEMPO- oxidized cellulose nanofibril composite films, *Cellulose*. 24 (2017) 4861–4870.
- [14] W.C.J. Zuiderduin, C. Westzaan, J. Huétink, R.J. Gaymans, Toughening of polypropylene with calcium carbonate particles, *Polymer*. 44 (2003) 261–275.
- [15] M. Henriksson, L.A. Berglund, P. Isaksson, T. Lindström, T. Nishino, Cellulose nanopaper structures of high toughness, *Biomacromolecules*. 9 (2008) 1579–1585.
- [16] H. Fukuzumi, T. Saito, T. Iwata, Y. Kumamoto, A. Isogai, Transparent and high gas barrier films of cellulose nanofibers prepared by TEMPO-mediated oxidation, *Biomacromolecules*. 10 (2009) 162–165.
- [17] T.C. Merkel, B.D. Freeman, R.J. Spontak, Z. He, I. Pinnau, P. Meakin, A.J. Hill, Ultrapervious, reverse-selective nanocomposite membranes, *Science*. 296 (2002) 519–522.
- [18] S. Hess, M.M. Demir, V. Yakutkin, S. Balushev, G. Wegner, Investigation of oxygen permeation through composites of PMMA and surface-modified ZnO nanoparticles, *Macromol. Rapid Commun.* 30 (2009) 394–401.

- [19] D. Liu, Y. Lv, M. Zhang, Y. Liu, Y. Zhu, R. Zong, Y. Zhu, Defect-related photoluminescence and photocatalytic properties of porous ZnO nanosheets, *J. Mater. Chem. A.* 2 (2014) 15377–15388.
- [20] F. Liu, Y.H. Leung, A.B. Djurišić, A.M.C. Ng, W.K. Chan, Native defects in ZnO : effect on dye adsorption and photocatalytic degradation, *J. Phys. Chem. C.* 117 (2013) 12218–12228.
- [21] D. Chen, Z. Wang, T. Ren, H. Ding, W. Yao, R. Zong, Y. Zhu, Influence of defects on the photocatalytic activity of ZnO, *J. Phys. Chem. C.* 118 (2014) 15300–15307.
- [22] S.C. Lyu, Y. Zhang, H. Ruh, H.J. Lee, H.W. Shim, E.K. Suh, C.J. Lee, Low temperature growth and photoluminescence of well-aligned zinc oxide nanowires, *Chem. Phys. Lett.* 363 (2002) 134–138.
- [23] K.K. Pandey, Study of the effect of photo-irradiation on the surface chemistry of wood, *Polym. Degrad. Stab.* 90 (2005) 9–20.
- [24] J.A. Olmstead, D.G. Gray, Fluorescence emission from mechanical pulp sheets, *J. Photochem. Photobiol. A: Chem.* 73 (1993) 59–65.
- [25] H. Tylli, I. Forsskåhl, C. Olkkonen, The effect of heat and IR radiation on the fluorescence of cellulose, *Cellulose.* 7 (2000) 133–146.
- [26] J. Cenens, R.A. Schoonheydt, Visible spectroscopy of methylene blue on hectorite, laponite B, and barasym in aqueous suspension, *Clays Clay Miner.* 36 (1988) 214–224.
- [27] K. Bergmann, C.T. O’Konski, A spectroscopic study of methylene blue monomer, dimer, and complexes with montmorillonite, *J. Phys. Chem.* 67 (1963) 2169–2177.

## Chapter 6

### Summary

Uniform ZnO/TOCN composite films were prepared using simple mixing procedures of the two components followed by casting and drying, in which different amounts or morphologies of ZnO nanoparticles were used. Multiple functions of the prepared nanocomposite films were characterized and studied, including optical, mechanical, thermal, hydrophilic, anti-microbial properties, as well as photocatalytic activity and oxygen permeability. Besides of this, two related subjects developed during the study of ZnO/TOCN nanocomposites, UV-induced degradation of TOCNs in water dispersions and influence of counter-ions of surface carboxylates of TOCNs on cell viability were also involved in this thesis.

First, ZnO/TOCN composite films with 0–50% ZnO contents were prepared by mixing ZnO/water and TOCN/ water dispersions at various weight ratios under the same stirring, sonicating, and subsequent casting and drying conditions. Fundamental, optical, thermal, surface wetting, mechanical, and antimicrobial properties were investigated in terms of ZnO contents. The ZnO/TOCN composite films showed characteristic UV-shielding properties with high light transparencies, depending on ZnO contents. The composite films had low CTEs ( $<10$  ppm/K), although the CTE value increased with increasing ZnO content probably because film porosities increased with ZnO content. In the case of composite films with high porosities, the films consisted of stiff TOCNs and ZnO particles and soft air components, the tensile strength and strain-to-failure decreased slightly with increasing ZnO content from 0 to 10%. The 50% ZnO-containing film had explicitly ductile properties because of its high porosity. Even though both TOCNs and ZnO particles are hydrophilic, the composite films exhibited various surface wettabilities, depending on the ZnO content. This behavior is explainable in terms of the surface roughness of the composite film or the presence of small air fractions on the film surface, according to Cassie's law. The ZnO/TOCN composite films displayed effective antibacterial activity, especially towards Gram-negative bacterium *Escherichia coli*. Any distinct improvement of thermal degradation point ( $T_d$ ) was not observed for the composite films; their weight decreases started at  $\sim 200$  °C in  $N_2$  atmosphere irrespective of the ZnO content.

Then, the influence of filler morphology on film properties of ZnO/TOCN nanocomposites was investigated. TOCNs and ZnO nanoparticles with different morphologies, i.e., spheres, rods, and needles, were mixed in water. The ZnO/TOCN mixtures were then cast and dried to prepare ZnO/TOCN (1:9 w/w) composite films to investigate the influence of ZnO nanoparticle morphology on composite film properties. The film densities varied from 1.25 to 1.63 g/cm<sup>3</sup> and porosities ranged from 5.4 vol% to 22 vol% depending on the morphology of ZnO nanoparticles. The (100) plane of the rod- and needle-like wurtzite ZnO particles were preferentially oriented to the composite film surface. The Young's modulus and tensile strength of the composite films were similar regardless of nanoparticle morphology, whereas the ZnO/TOCN films with higher porosities had greater elongations at break and works of fracture. The composite films consisting of rod- and needle-like ZnO particles had low oxygen permeability at 50% relative humidity. All the ZnO/TOCN composite films screened UV light, and the film containing spherical ZnO nanoparticle had the highest visible-light transmittance. The ZnO/TOCN composite films and their components showed photoluminescence when excited by UV light with the highest intensity at 370-nm UV light. The UV-induced ZnO-catalyzed degradation of methylene blue (MB) in water was restricted in the presence of TOCN, which may be caused by electrostatic interactions (or aggregation) between anionic TOCN elements and cationic MB molecules.

Since we found that TOCN is degraded by UV irradiation in the previous section, UV-degradation behavior of TOCN was investigated in detail. A softwood bleached kraft pulp was oxidized by the TEMPO/NaBr/NaClO system under different oxidation conditions to prepare TOCNs with various carboxylate contents. Water dispersions of these TOCNs were homogeneously subjected to UV irradiation experiment using a photochemical reactor equipped with a high pressure mercury lamp with the main wavelength of 365 nm. Changes in light transmittance and viscosity of the TOCN/dispersion and those in nanofiber morphology, functional groups, crystal structure, and molecular weight of the TOCNs were investigated in terms of UV-irradiation time and carboxylate content of TOCNs. Aqueous TOCN dispersions showed interesting changes in light transmittance and viscosity under different UV-irradiation time. As the UV-irradiation time was increased, the pH values of the dispersion decreased, showing some acid groups are formed from TOCN during UV irradiation. The weight recovery ratios of UV-treated TOCNs decreased with the UV-irradiation time, when the TOCNs were recovered as gels after addition of methanol to the UV-treated aqueous TOCN dispersion. Moreover, the average lengths and carboxylate contents of UV-treated TOCNs decreased with UV-irradiation time.

Because the pH values decreased for the UV-treated TOCN dispersions, some carboxylate groups were detached from TOCNs and simultaneously some new acid groups were formed as water/methanol-soluble low-molecular-weight compounds. The length of TOCN decreased to ~150 nm, which corresponds to the lengths of cellulose nanocrystals prepared by acid hydrolysis of plant celluloses. Molecular weights and molecular weight distributions of UV-treated TOCNs were analyzed by size-exclusion chromatography attached with multi-angle laser-light scattering (SEC-MALLS). The results showed that molecular weight of the original TOCN significantly decreased with UV-irradiation time; UV-induced depolymerization of TOCN molecules as well as shortening of TOCN length was achieved in this study. X-ray diffraction analysis of the UV-treated TOCNs showed that no significant decreases in crystallinity index or crystal width of celluloses I was observed.

Finally, TOCNs with different lengths and carboxylate contents and counter-ions of surface carboxylates were fabricated to investigate the influence of ions of CNF surfaces on cellular biocompatibility. Cellular biocompatibility of TOCNs with different counter-ions was investigated in terms of overall cell viability, all/dead cell population analysis, and intracellular changes of reactive oxygen species and mitochondrial mass and potential. TOCNs showed good cellular biocompatibility. When TOCNs with low carboxylate contents were used, the number of dead cells slightly increased. However, TOCNs with high carboxylate contents exhibited dead cell proportion at normal level. Counter-ions of TOCNs had some influences on biocompatibility. In particular, potassium counter-ion led to lower cellular biocompatibility than others.

## Publications

### Peer-reviewed journal articles

1) **Ruizhi Ning**, Chun-Nan Wu, Miyuki Takeuchi, Tsuguyuki Saito, Akira Isogai, “Preparation and characterization of zinc oxide/TEMPO-oxidized cellulose nanofibril composite films”, *Cellulose*, 2017, 24, 4861-4870.

2) **Ruizhi Ning**, Miyuki Takeuchi, Jin-Ming Lin, Tsuguyuki Saito, Akira Isogai, “Influence of the morphology of zinc oxide nanoparticles on the properties of zinc oxide/nanocellulose composite films”, *Reactive and Functional Polymers*, 2018, 131, 293-298.

(Reference articles)

3) **Ruizhi Ning**, Feng Wang, Ling Lin, “Biomaterial-based microfluidics for cell culture and analysis”, *Trends in Analytical Chemistry*, 2016, 80, 255-265.

4) Qichen Zhuang, **Ruizhi Ning**, Yuan Ma, Jin-Ming Lin, “Recent developments in microfluidic chips for in vitro cell-based research”, *Chinese Journal of Analytical Chemistry*, 2016, 44, 522-532

### International Conference

*Oral presentation*

1) **Ruizhi Ning**, Linglu Yi, Shunsuke Yamasaki, Jin-Ming Lin, Tsuguyuki Saito, Akira Isogai, “Cellular biocompatibility of TEMPO-oxidized cellulose nanofibers”, 253<sup>rd</sup> ACS National Meeting, San Francisco, USA, April 2-6, 2017.

*Poster presentation*

1) **Ruizhi Ning**, Chun-Nan Wu, Tsuguyuki Saito, Akira Isogai, “Preparation and characterization of composite films of zinc oxide nanoparticles and TEMPO-oxidized cellulose nanofibrils”, The 4th International Cellulose Conference, Fukuoka, Japan, October 17-20, 2017.

2) **Ruizhi Ning**, Linglu Yi, Akira Isogai, Jin-Ming Lin, “Cellular biocompatibility of TEMPO-oxidized cellulose nanofibers to human umbilical vein cells with different counter-ions”, The 8th International Conference on Materials Engineering for Resources, Akita, Japan, October 25-27, 2017.

### Domestic Conference

*Poster presentation*

1) **Ruizhi Ning**, Shunji Fujisawa, Tsuguyuki Saito, Akira Isogai, “Film properties of cellulose nanofiber and zinc oxide nanocomposites”, セルロース学会第 25 回年次大会, Kyoto, Japan, July 5-6, 2018.

2) **Ruizhi Ning**, Shunji Fujisawa, Tsuguyuki Saito, Akira Isogai, “Multifunctional ZnO/TOCN nanocomposite films and filler influences on the film properties”, CREST 研究の成果報告会, Tokyo, Japan, October 16, 2018.